Article

Boosting the Hydrodeoxygenation Activity and Selectivity of Ni/(M)-SBA-15 Catalysts by Chemical Alteration of the Support

Lina A. Calzada, Daniel Pérez-Estrada, Miriam Sánchez-Ramírez, Diana Gómora-Herrera, Antonio Gómez-Cortés, Gabriela Díaz, and Tatiana E. Klimova*
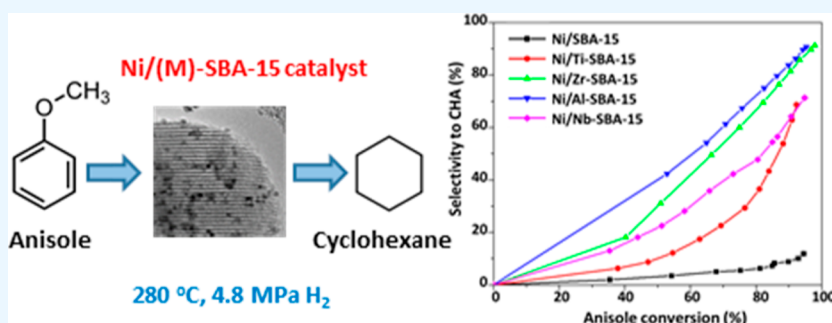
Read Online

ACCESS | Metrics & More | Article Recommendations | Supporting Information

ABSTRACT: The influence of the acid sites in the hydrodeoxygenation of anisole performed over Ni catalysts supported on SBA-15 modified with metal oxides (Ni/M-SBA-15, M = Ti, Zr, Al, or Nb) was demonstrated. Catalysts were characterized by SEM−EDX, nitrogen physisorption, XRD, UV−visible DRS, TPR, TPD of ammonia, IR-Py, O_2 chemisorption, and high-resolution transmission electron microscopy. The mesoporous structure and the hexagonal arrangement of the supports were maintained in the catalysts. Ni catalysts supported on modified M-SBA-15 exhibited a higher metal-support interaction, an increase in the acidity and, as a consequence, improved selectivity to cyclohexane. The deoxygenation reaction rate constants increased as Ni/SBA-15 < Ni/Ti-SBA-15 < Ni/Nb-SBA-15 < Ni/Zr-SBA-15 < Ni/Al-SBA-15, which is attributed to the increase in the amount and strength of acid sites, especially of the Brønsted ones, which promotes the cleavage of the C−O bond. It is also important to keep the metal/acid sites together to obtain high activity and selectivity to hydrodeoxygenated products.

1. INTRODUCTION

The ongoing global energy crisis, stemming from depletion and limited access to petroleum feedstocks, calls for the advancement of renewable energy sources. Biomass utilization to produce sustainable and renewable fuels has emerged as a promising solution to address energy problems. Fast pyrolysis of lignocellulosic biomass offers a high potential to generate bio-oils for producing various types of fuels. The starting biomass retains over 70% of its original energy content while containing considerably less nitrogen and sulfur compared to fossil fuels.[1] Nevertheless, bio-oils derived from fast pyrolysis exhibit a notable drawback in the form of a high oxygen content, reaching up to 40%. This characteristic renders them unsuitable for direct utilization in diesel engines due to their low calorific value, low pH (leading to increased corrosiveness), and high viscosity.[1−4]

Hydrodeoxygenation (HDO) is an efficient process performed at high temperatures and pressures to break the aromatic and aliphatic C−O bonds present in bio-oils, ultimately resulting in the removal of oxygen.[3,5] Furthermore, it is recognized that the HDO of phenolic compounds typically proceeds through two parallel reaction pathways: (a) cleavage

of the $C_{aromatic}$−O bond generating aromatic products and (b) hydrogenation of the aromatic ring before the rupture of the carbon−oxygen bond, resulting in the formation of saturated products.[1] The specific reaction pathway ultimately depends on the nature of the support and the active phase (reduced metal, metal phosphide, metal sulfide, etc.), which modify the catalyst's activity and selectivity.

Catalysts based on noble metals such as Pt, Pd, Rh, and Ru supported on different materials have been investigated in HDO of different model compounds, obtaining high yields of hydrocarbons.[6−15] Nickel-based catalysts are an alternative to noble metals, primarily due to their lower cost and high activity.[13,16,17] On the other hand, different kinds of ordered mesoporous materials, such as MCM-41, SBA-15, SBA-16, KIT-6, and others, have garnered significant attention as

supports for heterogeneous catalysts.[18−20] In the field of HDO of bio-oil model compounds, the use of different Ni catalysts supported on SBA-15-type materials has been reported in the literature. For instance, hydrotreating of a mixture of methyl esters was conducted over Ni and Co catalysts supported on SBA-15 and Al-SBA-15.[21] The presence of aluminum in the support favored the HDO process, achieving a higher selectivity and yield of C_{18} hydrocarbons than with SBA-15-based materials. Jin et al.[22] reported a better deoxygenation activity in HDO of anisole for Ni/SBA-15 and Ni/SiO₂ catalysts than for Ni supported on activated carbon. The high efficiency was attributed to the combination of acidic sites, which could contribute to the C−O bond scission and the good dispersion of metallic Ni particles. Yang et al.[23] investigated Ni catalysts employing different supports (SBA-15, Al-SBA-15, γ-Al₂O₃, microporous carbon, TiO₂, and CeO₂) for HDO of anisole. They observed very high HDO activity (in some cases ∼100%), concluding that the acidity of the support is very relevant for the hydrogenolysis of anisole, while metallic sites participate in the hydrogenation of intermediate compounds to yield cyclohexane (CHA). Ni and Co catalysts supported on hierarchical ZSM-5 and mesostructured SBA-15 and Al-SBA-15 were also evaluated in the HDO of anisole.[24] The results also showed a synergetic effect between the acidic sites of the supports and the metallic active phases, which favors the HDO of anisole. Gbadamasi et al.[25] found that Ni/Al-SBA-15 catalysts were promising for HDO of dibenzofuran (DBF) into hydrocarbons, observing a synergetic effect between Ni and the Al-SBA-15 support. Li et al. tested the performance of Ni/Al-SBA-15 catalysts in eugenol HDO and observed that the activity and selectivity of the catalysts were affected by both the quantity of acid sites and the dispersion of nickel species.[26,27] Finally, NiNb and Ni−ZrO₂ catalysts supported on SBA-15 silica also showed high activity in the HDO of anisole and guaiacol, respectively, with high selectivity toward CHA production.[28,29] The activity of the NiNb/SBA-15 was explained in terms of acidity, metal surface exposure, and reducibility as a function of the interaction between the phases present,[28] while the good activities and selectivities toward total deoxygenation obtained for the silica supported Ni−ZrO₂ catalysts were associated with the proximity between Ni and ZrO₂ particles when confined in the silica mesopores.[29] Summarizing the above results, it can be noted that, in general, bifunctional metal-acid catalysts show catalytic performance in HDO superior to that of their metallic counterparts supported on unmodified SBA-15 silica. The advantage of bifunctional metal-acid catalysts for HDO reactions is due to their ability for dissociation of hydrogen on the metal component and for "C−O" adsorption and activation on acid sites.[5] Nowadays, the introduction of different functionalities over mesoporous silica and their cooperation to achieve the catalytic turnover is well-known for different types of reactions.[18] However, for HDO reactions, in particular, only Ni catalysts supported on SBA-15 and Al-SBA-15 have been mainly studied, leaving insufficient information regarding the performance of similar catalysts supported on SBA-15 materials modified with other metal oxides.

In the present work, a comparison study of non-noble Ni catalysts supported on SBA-15 modified with different metal oxides (TiO₂, ZrO₂, Al₂O₃, and Nb₂O₅) was performed to contribute to the rational design of new low-cost bifunctional catalysts for HDO. Prepared catalysts were evaluated in the HDO of anisole as a probe molecule representative for lignin-derived bio-oils. Activity and selectivity trends were correlated with the characteristics of metallic and acidic sites with the intention of further investigating the participation of both of them in different steps of the HDO process. Special attention was placed on the characteristics of acidic sites (amount, type, and strength) and metal-support interaction in the catalysts.

2. EXPERIMENTAL SECTION

2.1. Preparation of SBA-15 and M-SBA-15 Supports.
The mesoporous SBA-15 support was synthesized according to the Zhao et al. procedure,[30] employing the triblock copolymer Pluronic P123 (M_{av} = 5800, EO₂₀PO₇₀EO₂₀) as a template and tetraethyl orthosilicate (TEOS, 98% Aldrich) as a silica source. The nominal molar ratio of the chemicals used in the synthesis was 1TEOS/0.017P123/5.95HCl/171H₂O. The hydrothermal treatment was performed first upon stirring at 35 °C (20 h) and then without stirring at 100 °C (24 h). The obtained solid product was washed with deionized water and air-dried at room temperature. The calcination step was performed in static air at 550 °C for 6 h. This SBA-15 silica was employed as a parent material to prepare supports modified on the surface with different metal oxides.

SBA-15 supports modified with TiO₂, ZrO₂, or Al₂O₃ were prepared by chemical grafting, while the Nb₂O₅-containing support was prepared by incipient wetness impregnation. The synthesized supports were denoted as M-SBA-15 (M = Ti, Zr, Al, or Nb). For chemical grafting, Ti(IV) isopropoxide (Ti(i-PrO)₄, Aldrich, 97%), Zr(IV) propoxide (Zr(n-PrO)₄, Fluka, 70 wt % solution in 1-propanol), and Al(III) chloride (AlCl₃, Sigma-Aldrich) were used as M precursors. An excess of M precursor (3.6 mmol per gram of SBA-15, which is equal to 3 M atoms per nm² of SBA-15 surface) was dissolved in absolute ethanol (100 mL, J.T. Baker), and then 1 g of SBA-15 was added to the solution and kept under magnetic stirring for 4 h at room temperature. After that, the solid material was filtered and vigorously washed with absolute ethanol to remove the unreacted precursor. The Al-SBA-15 support was also washed with abundant deionized water to remove chloride anions. Finally, the modified supports were dried at room temperature in air and calcined in static air at 550 °C for 5 h. The Nb-SBA-15 support was prepared by the impregnation of an aqueous solution of ammonium niobate(V) oxalate hydrate (NH₄[NbO(C₂O₄)₂](H₂O)ₙ, 99.99%, Sigma-Aldrich). The required amount of Nb precursor (0.61 mmol per gram of SBA-15) was used to obtain the nominal charge of Nb₂O₅ equal to 7.5 wt %. This Nb₂O₅ loading was selected to avoid the agglomeration of Nb₂O₅ on the SBA-15 surface, which was observed at higher loadings. The Nb-SBA-15 support was dried at room temperature overnight and then at 100 °C for 6 h in static air. The calcination step was performed at 500 °C for 5 h.

2.2. Preparation of Ni Catalysts.
Ni catalysts were prepared by incipient wetness impregnation of the (M)-SBA-15 supports with an aqueous solution of nickel nitrate (Ni(NO₃)₂·6H₂O, Sigma-Aldrich) containing the necessary amount to obtain a theoretical loading of 4 wt % of Ni. After impregnation, the catalysts were dried at 100 °C for 12 h and calcined at 500 °C for 2 h. The calcined catalysts were denoted as NiO/(M)-SBA-15 (M = Ti, Zr, Al, or Nb).

2.3. Characterization of Supports and Catalysts.
The chemical composition of supports and catalysts was obtained using scanning electron microscopy coupled to an energy-

dispersive X-ray analyzer (SEM−EDX) employing a JEOL 5900 LV microscope with Oxford ISIS equipment.

The textural properties of supports and catalysts were determined by N_2 physisorption employing a Micromeritics 3-FLEX automatic analyzer at a liquid N_2 temperature (−197.5 °C). Prior to the experiments, the samples were degassed at 270 °C under a N_2 flow for 12 h. Specific surface areas were calculated by the BET method (S_{BET}), while the total pore volumes (V_p) were determined by nitrogen adsorption at a relative pressure of 0.98. Pore size distributions were obtained from the adsorption and desorption isotherms by the BJH method. The mesopore diameters () (D_{ads} and D_{des}) correspond to the maxima of the pore size distributions obtained from the adsorption and desorption isotherms, respectively. The micropore area (S_μ) was estimated using the correlation of t-Harkins and Jura (t-plot method).

Powder X-ray diffraction (XRD) patterns were recorded on a Siemens D5000 diffractometer using CuK_α radiation (λ = 1.5406 Å) and a goniometer speed of 1° (2θ)/min in the 10 to 80° (2θ) range. Small-angle XRD (SA-XRD, 2θ = 0.5−10°) was performed on a Bruker D8 ADVANCE diffractometer using small divergence and scattering slits of 0.05°. The a_0 unit-cell parameter of SBA-15-type materials was estimated from the position of the (100) diffraction line as $a_0 = 2/\sqrt{3} \times d_{100}$. Pore wall thickness, δ, was assessed by subtracting D_{ads} from the a_0 unit-cell parameter, which corresponds to the distance between the centers of the adjacent mesopores.

UV−vis diffuse reflectance spectra (DRS UV−vis) of supports and catalysts were recorded in the wavelength range from 200 to 800 nm at room temperature by using a Varian Cary 100 Conc spectrophotometer equipped with a diffuse reflectance attachment. Polytetrafluoroethylene was employed as a reference.

Temperature-programmed reduction (TPR) and temperature-programmed desorption of ammonia (TPD-NH_3) profiles were obtained by using a Micromeritics AutoChem II 2920 automatic analyzer equipped with a thermal conductivity detector (TCD). Prior to the TPR analysis, 50 mg of sample was pretreated in situ at 400 °C for 2 h in an air flow and then cooled to room temperature under an Ar stream. The reduction step was performed from room temperature to 1000 °C (10 °C/min) under a H_2/Ar mixture flow (10:90 mol/mol, 50 mL/min). In the TPD-NH_3 experiments, 50 mg of sample was pretreated in situ at 500 °C for 30 min in a helium flow to remove water and other contaminants. Then, the samples were cooled to 120 °C and contacted with an NH_3/He mixture flow (10/90 mol/mol, 20 mL/min) for 30 min. The ammonia desorption step was performed in a He stream (50 mL/min) using a heating rate of 10 °C/min until reaching 500 °C, keeping this temperature until the trace reached the baseline.

The Fourier-transform infrared spectroscopy of adsorbed pyridine (Py-IR) was used to characterize acidic sites in the synthesized catalysts. For this study, the sample powders were pressed into self-supported thin wafers. IR spectra were recorded in absorption mode on a Thermo Scientific Nicolet 8700 spectrometer. Prior to the adsorption of pyridine, the samples were pretreated at 400 °C, with a heating rate of 20 °C/min, under vacuum for 45 min and cooled to room temperature. After pretreatment, the samples were exposed to saturated pyridine vapors for 20 min. After the adsorption of pyridine, the cell was evacuated, and the spectra were recorded after degassing at 50, 100, 200, 300, and 400 °C. The amount of adsorbed pyridine (coordinated or pyridinium ion) was estimated using the methods described by Hughes and White[31] and Emeis.[32]

Chemisorption of the O_2 was employed to determine the Ni dispersion of the reduced catalysts. The analyses were performed in a quartz tubular reactor equipped with a furnace with a thermocouple, a system for controlling temperature, and valves for gas pulses. Prior to the O_2 chemisorption, the samples (0.1 g) were reduced at 400 °C for 2 h under a H_2 flow (60 mL/min), followed by cooling to 25 °C in an Ar flow. The O_2 chemisorption was measured at 25 °C by introducing 1 mL of pulses of the O_2 (5%)/He into the argon flow. The pulses were continued, until no further uptake of O_2 was measured. The amount of chemisorbed O_2 on Ni atoms was determined with a HIDEN Analytical HPR-20 mass spectrometer following the signal of chemisorbed O_2 (m/z = 32). The amount of Ni atoms on the surface was calculated from the O_2 uptake by assuming an O/Ni atom of 1; meaning one O_2 molecule was chemisorbed with dissociation on two Ni surface atoms. The dispersion of metallic Ni (D) was the result of the ratio of the amount of Ni atoms on the surface determined by O_2 chemisorption to the total amount of Ni atoms in the sample, eq 1, determined by SEM−EDX

$$D = \frac{\text{Surface Ni}(\text{mol/g}_{cat})}{\text{Total Ni}(\text{mol/g}_{cat})} \times 100\% \tag{1}$$

High-resolution transmission electron microscopy studies were performed using a JEOL 2010 microscope (resolving power of 1.9 Å at 200 kV). The reduced catalysts were dispersed ultrasonically in heptane, and the suspension was collected on a carbon-coated grid.

2.4. Catalytic Activity Tests. The activation of the catalysts was performed prior to catalytic activity tests. For this, the NiO/(M)-SBA-15 catalysts were reduced ex situ in a U-shaped glass flow reactor at 400 °C under a stream of H_2/Ar (70:30 mol/mol) for 4 h at atmospheric pressure. Reduced catalysts were denoted as Ni/(M)-SBA-15 (M = Ti, Zr, Al, or Nb). The HDO of anisole was performed in a stainless steel batch reactor (300 mL, Parr) with a 0.36 M solution of anisole (Aldrich, 99%) in hexadecane (Aldrich, 99.5%). For each activity test, 50 mL of anisole solution and 100 mg of the reduced catalyst were used. The reaction conditions employed were 280 °C for 6 h with constant mechanical stirring (600 rpm). The reactor was filled with 3.5 MPa of hydrogen at room temperature, which gave 4.8 MPa total pressure at the reaction temperature (280 °C). Small aliquots of the reaction mixture (about 0.5 mL) were taken every 15 min during the first hour of the reaction and then hourly. The course of the reaction was followed by the analysis of aliquots in an Agilent 6890 gas chromatograph equipped with a flame ionization detector (FID) and a nonpolar methyl siloxane capillary column HP-1 (50 m × 0.32 mm inner diameter and 0.52 μm film thickness). Product identification was performed on an Agilent 7890 A GC system equipped with a 5975C MS detector.

Catalytic activity was determined by measuring the anisole concentration at different reaction times. The conversion of anisole (X_{AN}) was calculated as shown in eq 2, where C_0 is the initial anisole concentration (mol·L^{-1}) in the reaction mixture and C_{AN} is the concentration of anisole (mol·L^{-1}) at different reaction times (t, h)

$$X_{AN} = \left(\frac{C_0 - C_{AN}}{C_0} \right) \times 100\% \qquad (2)$$

The rate constants (k_1 and k_2) were determined assuming that the hydrogenation of anisole and deoxygenation of cyclohexyl methyl ether (CME) and cyclohexanol (CHL) are the pseudo-first order reactions (since H_2 is in large excess), based on the following simplified reaction scheme, eq 3

Anisole (AN) $\xrightarrow{k_1}$ Oxygenated intermediates (CME

$+$ CHL)

$\xrightarrow{k_2}$ Cyclohexane (CHA) $\qquad (3)$
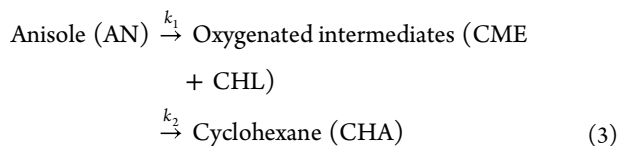
The rate constants k_1 and k_2 were calculated employing a curve-fitting method[33] for eqs 4−6, respectively

$$C_{AN} = C_0 e^{-k_1 t} \qquad (4)$$

$$C_{CME+CHL} = \frac{k_1 C_0}{k_2 - k_1}[e^{-k_1 t} - e^{-k_2 t}] \qquad (5)$$

$$C_{CHA} = \frac{C_0}{k_2 - k_1}[k_2(1 - e^{-k_1 t}) - k_1(1 - e^{-k_2 t})] \qquad (6)$$

Selectivity to CHA (S_{CHA}) was defined as the CHA content (%) in the reaction mixture.

3. RESULTS

3.1. Characterization of Supports and Calcined Catalysts.
The chemical compositions of the supports and catalysts were determined by SEM−EDX analysis. Table 1

Table 1. Chemical Composition of the Synthesized Supports and Catalysts Was Determined by SEM−EDX

sample	experimental loading (wt %)				
	Ni[a]	NiO	metal (M)[b]	M_xO_y[c]	M atoms/nm²
			Support		
Ti-SBA-15			8.3	13.8	2.00
Zr-SBA-15			13.0	17.6	1.74
Al-SBA-15			1.9	3.5	0.69
Nb-SBA-15			4.4	6.3	0.45
			Catalyst		
NiO/SBA-15	4.0	5.1			
NiO/Ti-SBA-15	3.6	4.6	7.8	13.1	2.04
NiO/Zr-SBA-15	3.9	5.0	12.9	17.4	1.96
NiO/Al-SBA-15	3.8	4.8	1.6	3.0	0.60
NiO/Nb-SBA-15	4.0	5.1	4.3	6.2	0.50

[a]Nominal loading of Ni was 4.0 wt %. [b]M, metal deposited on the SBA-15 surface (M = Ti, Zr, Al, and Nb). [c]M_xO_y = TiO$_2$, ZrO$_2$, Al$_2$O$_3$, and Nb$_2$O$_5$.

shows that the SBA-15 supports modified by chemical grafting of Ti, Zr, and Al oxides exhibited 13.8, 17.6, and 3.5 wt % of the respective metal oxide, while the Nb-containing SBA-15 supports showed 6.3 wt % of Nb$_2$O$_5$, a value close to the theoretically expected (7.5 wt %). The surface density of metal atoms in the M-SBA-15 supports was between 0.45 and 2.0 M atoms per nm^2. The experimentally determined loadings of metal Ni catalysts were found between 3.6 and 4.0 wt % (Table 1), quite close to the expected value (4 wt %).

Figure 1 shows elemental mapping images of a selected NiO/Al-SBA-15 catalyst. It was observed that both Al and Ni species showed good dispersion and a homogeneous distribution in this calcined catalyst. Elemental mappings of other prepared catalysts shown in the Supporting Information, Figure S1, also confirmed the homogeneous distribution of nickel species and metal oxides in the catalysts.

Figure 2a shows the nitrogen adsorption−desorption isotherms of the (M)-SBA-15 supports. They all correspond to a type IV, characteristic of mesoporous materials, with an H1 hysteresis loop, typically associated with uniform cylindrical mesopores. After the incorporation of Ti, Zr, Al, and Nb oxides into the SBA-15 support, the shapes of the adsorption−desorption isotherms and hysteresis loops were preserved. Figure 2b,c, shows the pore size distributions of the supports, obtained from the adsorption and desorption branches of the isotherms, respectively. All the materials presented well-defined monomodal pore size distributions. The SBA-15 silica showed mesopore distributions with maxima centered at 91 Å (adsorption) and at 67 Å (desorption). The modified M-SBA-15 supports presented slightly broader pore size distributions, with a slight decrease in the maximum pore size. This decrease could be attributed to the deposition of Ti, Zr, Al, and Nb oxides inside the mesopore channels of the parent SBA-15 material.

The textural characteristics of the prepared supports are listed in Table 2. The SBA-15 material exhibited the highest specific surface area (722 m^2/g) and pore volume (1.24 cm^3/g), while the Ti-, Zr-, Al-, and Nb-containing supports showed decreased surface areas (631 to 495 m^2/g) and pore volumes (1.12 to 0.83 cm^3/g) due to the incorporation of nonporous metal oxides.

A stronger change in the adsorption and desorption pore diameters was observed for the supports modified with TiO$_2$ and ZrO$_2$ species (Table 2), probably due to a larger amount of these oxides grafted on the SBA-15 surface (Table 1). The calcined NiO/(M)-SBA-15 catalysts did not show significant changes in the shape of adsorption−desorption isotherms and hysteresis loops (Supporting Information, Figure S2), compared to the corresponding supports, nor in pore size distributions. The addition of about 5 wt % of nickel oxide to the (M)-SBA-15 supports, as expected, resulted in a slight decrease in the specific textural characteristics of the catalysts (S_{BET} and V_p), without significant changes in the pore diameter values (Table 2). These results indicate that the characteristic mesopore structure of the starting SBA-15 support was maintained in the supports modified with Ti, Zr, Al, and Nb oxides, as well as in the calcined NiO/(M)-SBA-15 catalysts.

The SA-XRD patterns of the (M)-SBA-15 supports and calcined Ni catalysts (Supporting Information, Figure S3) showed three well-defined peaks located at approximately 0.9, 1.6, and 1.8° (2θ), associated with the (1 0 0), (1 1 0), and (2 0 0) characteristic reflections of the *p6mm* hexagonal symmetry of cylindrical mesopores of the SBA-15 material.[30] The hexagonal unit cell parameter (a_0) and the pore wall thickness (δ) of the samples were calculated based on the position of the most intense (1 0 0) reflection and adsorption pore diameter determined by N$_2$ physisorption (Table 2). The results are in agreement with the literature. All the samples showed similar a_0 values (between 111 and 114 Å). However, the pore wall thickness of the materials slightly increased after the incorporation of Ti, Zr, Al, and Nb oxides to the starting SBA-15 support as a result of the incorporation of the metal
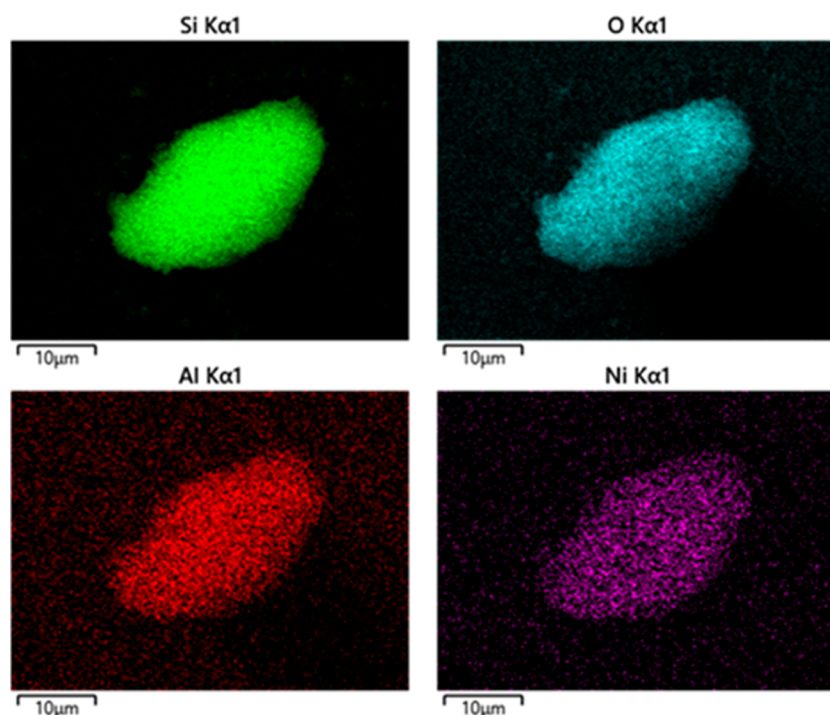
Figure 1. SEM−EDX images of the calcined NiO/Al-SBA-15 catalyst.
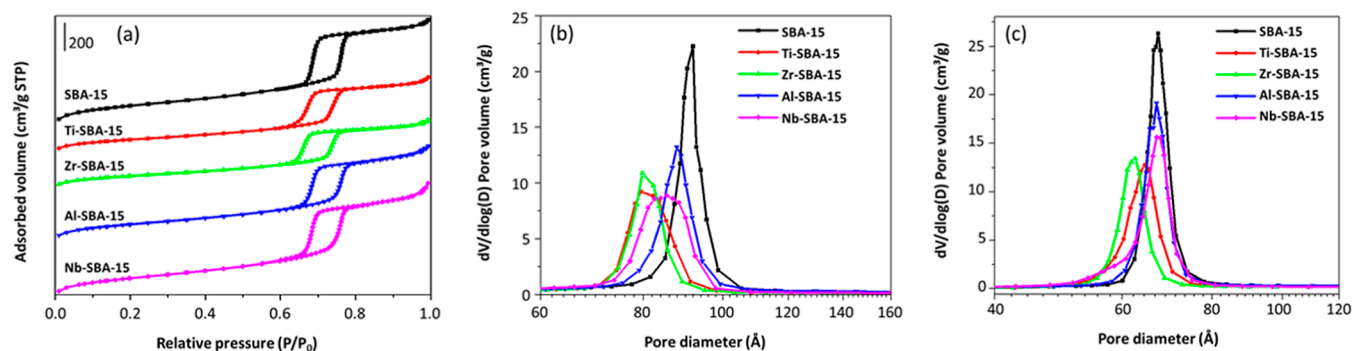

Figure 2. Nitrogen adsorption−desorption isotherms (a) and pore size distributions of supports: (b) adsorption and (c) desorption.

Table 2. Textural[a] and Structural[b] Characteristics of the Synthesized Supports and Calcined Catalysts

sample	S_{BET} (m²/g)	V_p (cm³/g)	S_μ (cm³/g)	D_{ads} (Å)	D_{des} (Å)	a_0 (Å)	δ (Å)
			Support				
SBA-15	722	1.24	0.026	91	67	114	23
Ti-SBA-15	520	0.91	0.030	80	65	112	32
Zr-SBA-15	495	0.83	0.025	80	63	111	31
Al-SBA-15	612	1.12	0.007	88	67	112	24
Nb-SBA-15	631	1.07	0.034	86	67	111	25
			Catalyst				
NiO/SBA-15	610	1.04	0.018	87	65	114	27
NiO/Ti-SBA-15	481	0.85	0.023	78	64	111	33
NiO/Zr-SBA-15	434	0.75	0.023	80	63	111	31
NiO/Al-SBA-15	590	1.05	0.021	87	68	112	25
NiO/Nb-SBA-15	555	1.03	0.016	86	67	111	25

[a]S_{BET}, specific surface area; V_p, total pore volume; S_μ, micropore area; and D_{ads} and D_{des}, mesopore diameters corresponding to the maximum of the pore size distributions calculated from the adsorption and desorption isotherms, respectively, by the BJH method. [b]a_0, unit-cell parameter calculated from the position of the (100) diffraction peak ($a_0 = 2/\sqrt{3} \times d_{100}$) and δ, pore wall thickness of SBA-15 materials calculated by the subtraction of pore diameter (D_{ads}) from the unit cell parameter a_0.

oxide inside the mesopore channels covering their walls.[34] This effect was stronger for the TiO₂- and ZrO₂-containing

supports. On the other side, after the incorporation of nickel species to the supports, the pore wall thickness almost did not
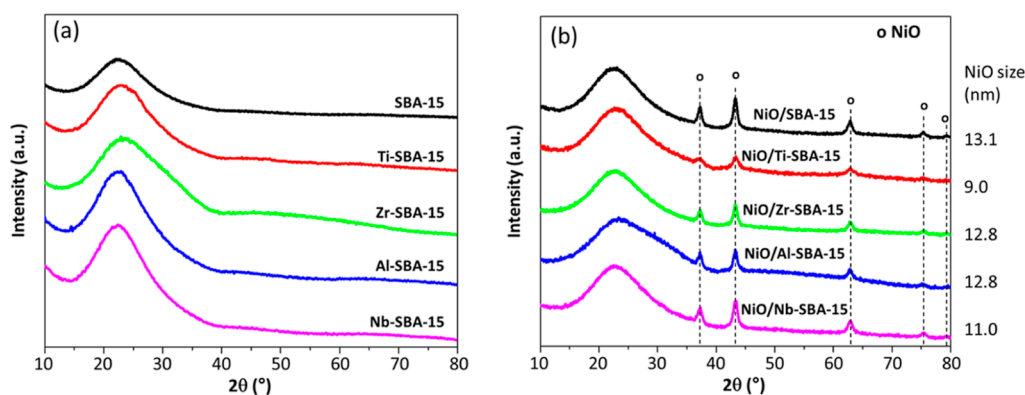
Figure 3. Powder XRD patterns of (a) supports and (b) calcined catalysts. Crystalline phase detected: cubic NiO (ICDD 01-071-1179).

change in the calcined NiO/(M)-SBA-15 catalysts compared to the corresponding supports. This can be due to the good dispersion of the nickel oxide species located inside the mesopores in the calcined catalysts or to the agglomeration of the deposited NiO species on the external surface of the (M)-SBA-15 supports.

Figure 3a shows the powder XRD patterns of the starting SBA-15 and M-SBA-15 supports. In all cases, only one wide signal between 15 and 35° (2θ) was observed, attributed to the amorphous SiO_2 of the SBA-15 material. The absence of the reflection peaks corresponding to the deposited metal oxides (TiO_2, ZrO_2, Al_2O_3, and Nb_2O_5) in the diffractograms of the M-SBA-15 supports indicates that the respective metal oxide was well dispersed on the surface of the parent SBA-15. On the other side, in the powder XRD patterns of the calcined NiO/(M)-SBA-15 catalysts, Figure 3b, in addition to the same broad signals of amorphous silica, 15−35° (2θ), five new diffraction signals were detected at 37.2, 43.3, 62.9, 75.4, and 79.4° (2θ), associated with the (1 1 1), (2 0 0), (2 2 0), (3 1 1), and (2 2 2) planes, respectively, of cubic NiO crystalline phase (ICDD 01-071-1179). This result points out the presence of NiO crystals in all synthesized catalysts supported on (M)-SBA-15 materials.

The size of the NiO crystallites in the calcined catalysts was estimated from the width at half height of the more intense (2 0 0) reflection peak in the XRD patterns using the Scherrer equation. The largest NiO crystallites (13.1 nm) were observed in the catalyst supported on the pristine SBA-15, Figure 3b, which is reasonable due to the inert surface of this support leading to a very low metal-support interaction (MSI). For the calcined NiO catalysts supported on modified M-SBA-15 materials, the NiO size was slightly smaller, evidencing an increase in the MSI with the SBA-15 materials modified with different metal oxides (TiO_2, ZrO_2, Al_2O_3, and Nb_2O_5). It is worth mentioning that the size of the NiO crystallites detected in all catalysts by powder XRD (9.0 to 13.1 nm) is larger than the pore size of the (M)-SBA-15 supports (Table 2) so these NiO crystallites are probably located on the external surface of the mesoporous supports.

The reduction behavior of nickel oxide species in the calcined NiO/(M)-SBA-15 catalysts was investigated by TPR with H_2. Figure 4 shows the TPR profiles of the calcined catalysts.

The NiO/SBA-15 catalyst showed a broad reduction peak from 270 to 450 °C, with a maximum at 332 °C and a shoulder at ~415 °C. Since the reduction of the NiO species occurs in a single step (NiO + H_2 → Ni + H_2O), the presence of two
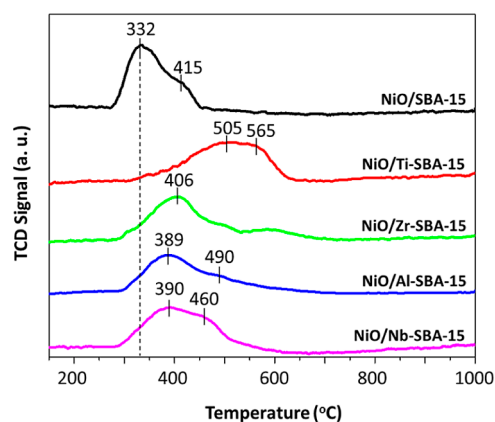

Figure 4. TPR profiles of the calcined catalysts.

overlapping signals in the TPR profile indicates the reduction of two different NiO species. Thus, the first peak is related to the reduction of the NiO particles on the external surface of the SBA-15 support, while the shoulder at a higher temperature is due to the reduction of NiO particles located in the interior of the mesoporous channels of the SBA-15. These species are more difficult to reduce due to a stronger interaction with the silica support.[35−37] On the other side, the NiO catalysts supported on the SBA-15 supports modified with different oxides (TiO_2, ZrO_2, Al_2O_3, and Nb_2O_5) showed broader peaks shifted to higher temperatures compared to the NiO/SBA-15 catalyst (Figure 4), indicating a stronger interaction between the NiO particles and the supports covered with the respective metal oxide.[23] Moreover, it must be pointed out that in the TPR profiles of NiO/Ti-SBA-15 and NiO/Nb-SBA-15, the high-temperature shoulder was more intense than that in the calcined NiO catalysts deposited on Zr- and Al-SBA-15 supports. This result indicates that the first two catalysts (NiO/Nb-SBA-15 and especially the NiO/Ti-SBA-15 catalyst) have a larger proportion of nickel oxide species located inside the mesoporous structure of the support than other calcined catalysts. This can be due to a stronger MSI with Nb- or Ti-containing supports that, on the one side, promotes NiO dispersion inside the mesopores and, on the other side, makes the reduction of such species more difficult. According to the NiO crystallite size determined by the Scherrer's equation, Figure 3b, these two catalysts (NiO/Ti-SBA-15 and NiO/Nb-SBA-15) also showed a smaller size of the NiO crystallites located on the external surface of the modified SBA-15 supports (9 and 11 nm, respectively) than in

other samples. The stronger interaction between NiO species and the metal oxide-containing SBA-15 supports also resulted in a slightly lower degree of reduction of the nickel oxide species in the NiO/M-SBA-15 catalysts compared with the NiO/SBA-15 catalyst (Table 3).

Table 3. Hydrogen Consumption and Degree of Reduction (α) of the Calcined Catalysts

| catalyst | T_{max} (°C)[a] | hydrogen consumption (μmol/g$_{cat}$) | | α[b] |
		theoretical	experimental	
NiO/SBA-15	332	15.26	15.05	0.99
NiO/Ti-SBA-15	505	13.74	12.78[c]	0.93[c]
NiO/Zr-SBA-15	406	14.88	13.45	0.96
NiO/Al-SBA-15	389	14.48	13.13	0.92
NiO/Nb-SBA-15	390	15.26	14.81	0.97

[a]T_{max}, temperature of the maximum of the main reduction peak. [b]α, degree of reduction determined as a ratio of hydrogen consumed by each catalyst to the theoretical hydrogen consumption, calculated based on the experimentally determined NiO loadings (Table 1). [c]Subtracting hydrogen consumption due to the reduction of the TiO$_2$-containing support.

UV−vis DRS of SBA-15 and modified supports are displayed in Figure 5a. The SBA-15 and Al-SBA-15 supports exhibited very low-intensity signals in the UV region. This could be caused by the presence of impurities. It is known that SiO$_2$ and γ-Al$_2$O$_3$ materials possess wide band gaps of 9.0 and 8.8 eV,[38,39] respectively. On the other hand, Ti-SBA-15, Zr-SBA-15, and Nb-SBA-15 supports showed intense signals in the UV region. The maxima of the absorption bands were observed at 238 and 227 nm for the Ti- and Nb-containing supports, respectively, which are related to the ligand-metal charge transfer (LMCT) from the O^{2-} to the Ti^{4+} and Nb^{5+} cations with a tetrahedral and pentahedral coordination, respectively.[34,40] The Zr-SBA-15 support showed the maximum of the absorption band at 243 nm, related to the LMCT from O^{2-} to Zr^{4+} cations with full connectivity of Zr−O−Zr.[34,41]

Figure 5b shows UV−vis DRS recorded for the calcined catalysts. The absorption band at ∼290 nm observed in the Ni/SBA-15, Ni/Zr-SBA-15, and Ni/Al-SBA-15 catalysts could be associated to the LMCT from the oxygen 2p orbitals to the nickel Eg orbital with NiO in octahedral coordination.[42,43] In Ni/Ti-SBA-15 and Ni/Nb-SBA-15, this band was not visible

due to the overlap with the LMCT from the respective metal oxide. Additionally, all the catalysts exhibited signals at ∼430 and ∼730 nm, ascribed to the spin-allowed transitions v$_3$ $^3A_{2g}$ (^3F) → $^3T_{1g}$ (^3P) and v$_2$ $^3A_{2g}$ (^3F) → $^3T_{1g}$ (^3F), respectively, for d−d transitions from the octahedrally coordinated nickel.[42] The signals at about 380 and 460 nm are related to the spin-forbidden transitions $^3A_{2g}$ (^3F) → $^1A_{1g}$(D) and $^3A_{2g}$ (^3F) → $^1T_{2g}$, respectively, due to the specific spin−orbit couplings and antiferromagnetic interactions in Ni(II) ions.[42]

TPD of ammonia (TPD-NH$_3$) and IR spectroscopy of the adsorbed pyridine (Py-IR) were used to characterize the acidity of supports and catalysts. Ammonia TPD was carried out to quantify the amount and classify the acid sites by their strength, but without distinguishing between Brønsted and Lewis acidity, while the Py-IR was used to characterize separately the Brønsted and the Lewis acid sites. The TPD of the ammonia profiles of supports and catalysts is shown in the Supporting Information, Figures S4a,b. Table 4 shows the results of the quantification of acid sites of different strengths in the supports and catalysts. The strength of the acid sites was determined based on the temperature of ammonia desorption. Thus, all the sites were divided into weak (120−200 °C), medium (200−350 °C), and strong (350−500 °C) ones.

It can be observed (Figure S4a and Table 4) that, as expected, the starting SBA-15 material showed the lowest total amount of acid sites, compared to the SBA-15 supports modified with different metal oxides (TiO$_2$, ZrO$_2$, Al$_2$O$_3$, and Nb$_2$O$_5$). The total amount of acid sites in the supports, as well as the surface density of the acid sites, increased as follows: SBA-15 ≪ Al-SBA-15 ≈ Nb-SBA-15 < Zr-SBA-15 < Ti-SBA-15, being the Ti-containing support the most acid. The medium strength acid sites were predominant in all the M-SBA-15 supports, followed by the weak and strong ones (Table 4). Therefore, as expected, the incorporation of the selected metal oxides on the SBA-15 surface produced a considerable increase in the acidity of the supports. The addition of NiO to the supports produced some changes in the acidity of the samples. The ammonia TPD profiles of the catalysts are shown in Figure S4b. It can be observed that the NiO/SBA-15 catalyst continued being the sample with the lowest total amount of acid sites among all the calcined catalysts. However, the total amount of acid sites and the surface density of acid sites increased somewhat differently from what was observed for the supports: NiO/SBA-15 ≪ NiO/Nb-SBA-15 < NiO/Ti-SBA-15 < NiO/Al-SBA-15 < NiO/Zr-SBA-15. In this case, the
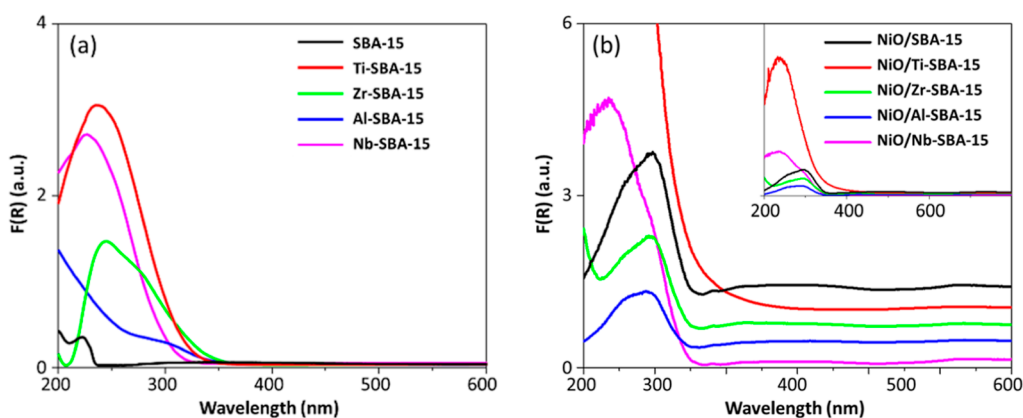

Figure 5. UV−visible diffuse reflectance spectra of (a) supports and (b) calcined catalysts.

Table 4. Results from the Characterization of the Supports and Calcined Catalysts by the TPD of Ammonia

| catalyst	acid sites (μmol NH_3/g)				density of acid sites (μmol NH_3/m^2)
	weak (120−200 °C)	medium (200−350 °C)	strong (350−500 °C)	total	
SBA-15	3	19	7	29	0.04
Ti-SBA-15	131	370	56	557	1.07
Zr-SBA-15	62	329	32	423	0.85
Al-SBA-15	43	189	31	263	0.43
Nb-SBA-15	56	177	39	272	0.43
NiO/SBA-15	6	20	14	40	0.06
NiO/Ti-SBA-15	136	125	18	279	0.58
NiO/Zr-SBA-15	150	238	43	431	0.99
NiO/Al-SBA-15	125	199	57	381	0.65
NiO/Nb-SBA-15	64	95	41	200	0.36
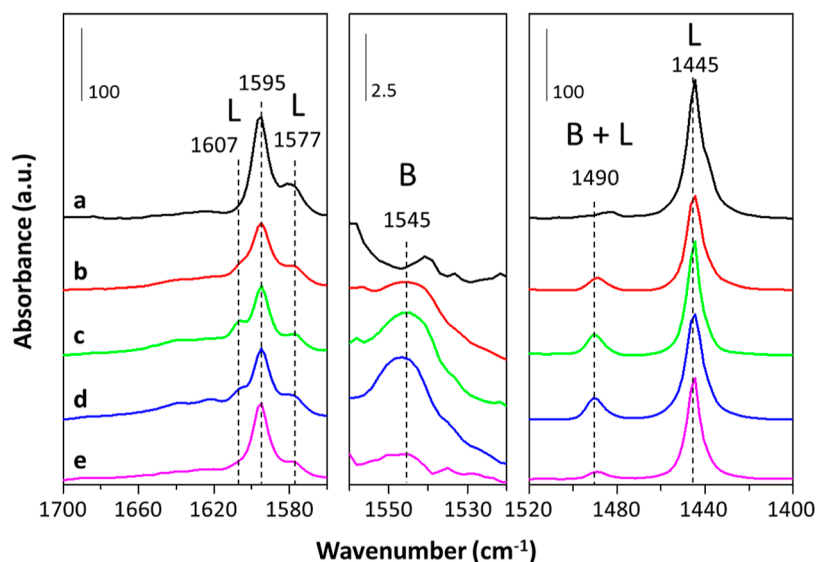
Figure 6. FT-IR spectra of pyridine adsorbed on the catalysts at 50 °C: (a) NiO/SBA-15, (b) NiO/Ti-SBA-15, (c) NiO/Zr-SBA-15, (d) NiO/Al-SBA-15, and (e) NiO/Nb-SBA-15. Intensity was normalized by the amount of the catalyst employed for each analysis.

NiO/Zr-SBA-15 and NiO/Al-SBA-15 catalysts showed larger acidity than the other three catalysts (Table 4). All the catalysts, as well as the corresponding supports, have predominantly weak and medium-strength acid sites but few strong ones. The amount of strong acid sites increased as follows: NiO/SBA-15 < NiO/Ti-SBA-15 < NiO/Nb-SBA-15 < NiO/Zr-SBA-15 < NiO/Al-SBA-15. The addition of NiO on the Ti-SBA-15, Zr-SBA-15, and Nb-SBA-15 supports, in general, resulted in an increase in the amount of weak acid sites in the catalysts, with a considerable decrease in the amount of medium-strength acid sites. This effect was much stronger for the Ti-containing support and catalyst, where the amount of medium-strength acid sites decreased from 370 to 125 μmol NH_3/g (almost 3-fold). On the other side, for the NiO/Al-SBA-15 catalyst, the amount of strong acid sites slightly increased after the incorporation of NiO to the Al-SBA-15 support. The trends in the acidity of the calcined catalysts could be the result of both the acidity of the supports modified with different metal oxides (TiO$_2$, ZrO$_2$, Al$_2$O$_3$, and Nb$_2$O$_5$) and the presence of the NiO species. The nickel oxide species, on the one side, could interact with the acid sites of the metal oxides deposited on the SBA-15 surface, covering the surface with well-dispersed NiO particles, decreasing the amount of acid sites; and, on the other side, some new acid sites could be created on the surface of the NiO particles. This

supposition is in line with the results obtained by TPR of the NiO/(M)-SBA-15 catalysts, which showed that the temperature of the reduction of NiO species strongly depends on the chemical composition of the (M)-SBA-15 support used. In this sense, the high temperature required for the reduction of NiO deposited on the Ti-SBA-15 support (400−630 °C, Figure 4) points out the strong interaction of the NiO species with this metal oxide. The same strong MSI could be the reason for a noticeable decrease in the amount of medium and strong acid sites in the NiO/Ti-SBA-15 catalyst.

IR spectroscopy of Py adsorbed at different temperatures (Py-IR) was used to obtain more information about the Brønsted (B) and Lewis (L) acid sites in the catalysts. Pyridine, as a strong base, interacts with B and L acid sites, forming different adsorbed structures that allow one to distinguish and quantify Py molecules adsorbed at different types of acid sites. Figure 6 shows the IR spectra of pyridine chemisorbed on the surface of the catalysts after degassing at 50 °C. A signal at ~1545 cm^{-1} corresponds to pyridine adsorbed on the B acid sites, where a pyridinium ion (PyH$^+$) is formed as a result of the protonation of the nitrogen atom of the Py molecule with the acidic proton. The coordination of Py to the L acid sites generally occurs through charge donation from the pair of electrons of nitrogen to the coordinatively unsaturated cations (L acid sites) exposed on the surface

Table 5. Results from the Characterization of the Calcined Catalysts by FT-IR of Adsorbed Py

samples	$T_{Py\ des}$ (°C)[a]	acid sites (μmol Py/g)				density of acid sites (μmol Py/m^2)
		Brønsted	Lewis	total	B/L	
NiO/SBA-15	50	0	2029	2029	0	3.33
	200	0	15	15	0	0.02
	400	0	0	0	0	0
NiO/Ti-SBA-15	50	25	1393	1418	0.018	2.95
	200	6	16	22	0.375	0.05
	400	1	0	1		0
NiO/Zr-SBA-15	50	64	1412	1476	0.045	3.40
	200	24	167	191	0.144	0.44
	400	0	0	0	0	0
NiO/Al-SBA-15	50	68	1642	1710	0.038	2.89
	200	34	230	264	0.148	0.45
	400	0	68	68	0	0.12
NiO/Nb-SBA-15	50	4	1289	1293	0.003	2.33
	200	0	30	30	0	0.05
	400	0	0	0	0	0

[a]Temperature of pyridine desorption. Acid sites were classified as weak, medium, and strong according to the temperature of Py desorption: 50, 200, and 400 °C, respectively.

(PyL). These signals are situated at ~1445 and ~1607 cm^{-1}, for strong L acid sites, and ~1577 cm^{-1} for weak L acid sites. The band at 1490 cm^{-1} is due to both L and B acid sites.[44−46] The amount of pyridine adsorbed on the B and L acid sites as a function of the temperature (Supporting Information, Figure S5) was determined following the bands at 1545 and 1445 cm^{-1}, respectively. It can be seen in the spectra shown in Figure 6, that for all the catalysts, the band of Py adsorbed at the L acid sites was much more intense than that of Py adsorbed at the B ones, indicating a higher concentration of L acid sites. The spectrum of the NiO/SBA-15 catalyst showed the highest initial amount of Py (50 °C) adsorbed on L acid sites, followed by NiO/Al-SBA-15, NiO/Zr-SBA-15, NiO/Ti-SBA-15, and NiO/Nb-SBA-15. After the degassing temperature was increased to 200 °C, the amounts of Py adsorbed at different acid sites drastically decreased (Figure S5). At this temperature, pyridine bonded to weak B and L acid sites was desorbed, and the signals still remaining in the IR spectra correspond to Py chemisorbed at medium and strong acid sites. The results from the quantification of B and L acid sites at different temperatures of Py desorption are shown in Table 5.

It can be clearly seen that the total amount of acid sites significantly decreased with increasing degassing temperature from 50 to 200 °C. According to an increase in the amount of medium and strong acid sites of both types (B + L), the catalysts can be ordered as NiO/SBA-15 < NiO/Ti-SBA-15 < NiO/Nb-SBA-15 ≪ NiO/Zr-SBA-15 < NiO/Al-SBA-15. The amount of medium and strong L acid sites changes in the same order, while the presence of medium and strong B acid sites was observed only in three catalysts, increasing their amount from NiO/Ti-SBA-15 to NiO/Zr-SBA-15 and NiO/Al-SBA-15. Additionally, it is important to note that after degassing at 200 °C, the NiO/SBA-15 catalyst did not show the presence of B acid sites, exhibiting exclusively only a small amount of L acid sites. After desorption of Py at 400 °C, no strong B acid sites were detected in all the catalysts. The NiO/Al-SBA-15 catalyst was the only one that showed the presence of strong L acid sites, where Py was still observed after desorption at 400 °C.

3.2. Characterization of Reduced Catalysts. Reduced catalysts were characterized by powder XRD, TEM, and O$_2$ chemisorption in order to obtain information about the characteristics of the metal active phase tested in the HDO of anisole. For these characterizations, calcined catalysts were reduced under the same conditions as those used for catalytic activity tests (400 °C, H$_2$/Ar flow, 4 h). The powder XRD profiles of the reduced catalysts (Figure 7) showed three
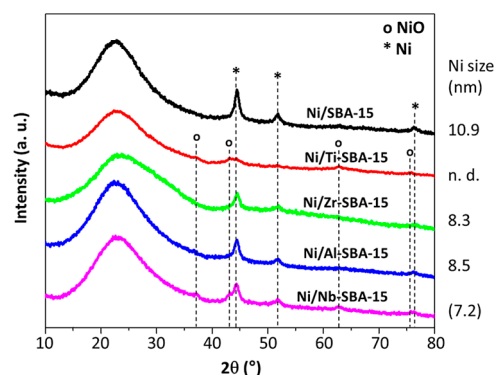

Figure 7. Powder XRD patterns of the reduced catalysts. Crystalline phases detected: cubic NiO (ICDD 01-071-1179) and cubic Ni (ICDD 01-071-4655).

diffraction peaks at 44.7, 51.8, and 76.8° (2θ), corresponding to the (1 1 1), (2 0 0), and (2 2 0) crystalline planes of the cubic phase of metallic Ni (ICDD 01-071-4655). This crystalline phase was detected in the diffraction patterns of all reduced catalysts. However, for the Ni/Ti-SBA-15 catalyst, the signals of the metallic Ni were much smaller in intensity and less defined than in the patterns of all other reduced catalysts. Metallic Ni was the unique crystalline phase detected in the diffraction patterns of the reduced Ni/SBA-15, Ni/Zr-SBA-15, and Ni/Al-SBA-15 catalysts.

The Ni crystallite sizes estimated for these catalysts using the Scherrer equation for the most intense diffraction peak at 44.7° (2θ) were 10.5, 8.3, and 8.5 nm, respectively (Figure 7). For the Ni/Nb-SBA-15 catalyst, the metallic Ni crystallite size was roughly estimated as 7.2 nm, while for the Ni/Ti-SBA-15
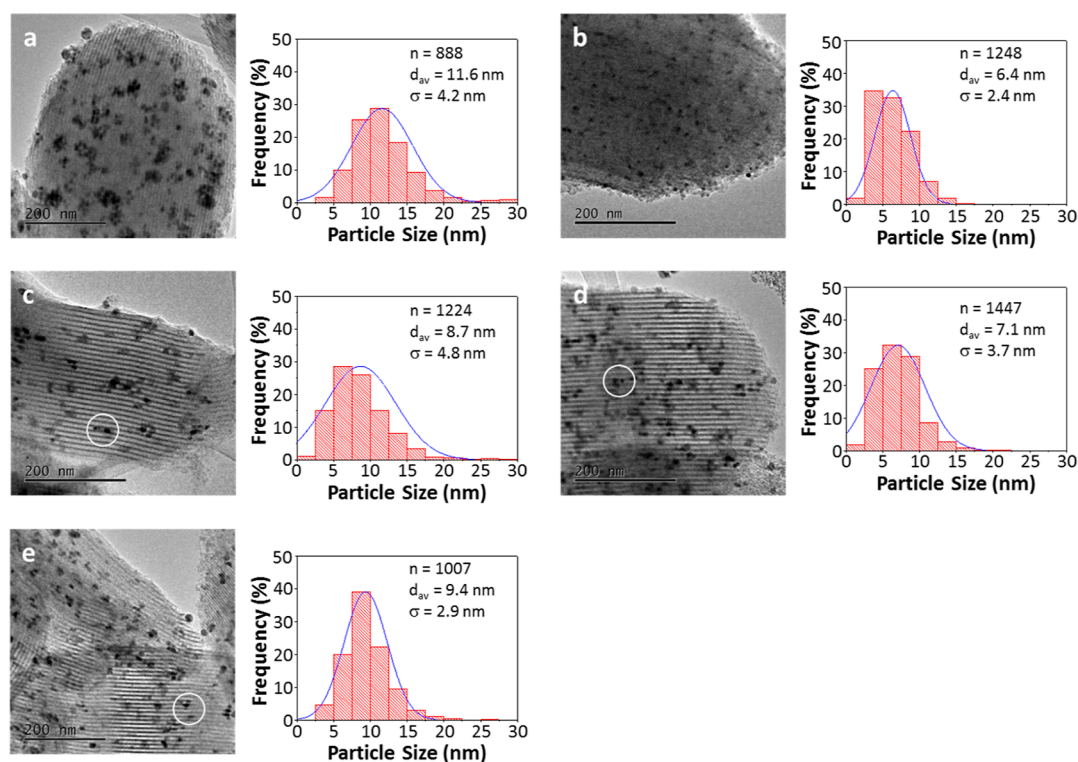
Figure 8. TEM images of reduced catalysts and particle size distributions: (a) Ni/SBA-15, (b) Ni/Ti-SBA-15, (c) Ni/Zr-SBA-15, (d) Ni/Al-SBA-15, and (e) Ni/Nb-SBA-15.

sample, it was not possible to estimate the Ni crystallite size based on the XRD data. It is important to note that the addition of the selected metal oxides to the SBA-15 support helps to increase the dispersion of metallic Ni nanocrystals in the reduced catalysts as well as of the NiO crystallites in the calcined precursors, Figure 3b. On the other hand, in the diffraction patterns of the Ni/Ti-SBA-15 and Ni/Nb-SBA-15 catalysts, in addition to the characteristic signals of the metallic Ni, other signals were detected at 37.2, 43.2, 62.9, and 75.4° (2θ) corresponding to the presence of the cubic crystalline phase of NiO (ICCD 01-071-1179). The presence of the NiO phase in these two catalysts, even after the reduction performed at 400 °C for 4 h, indicates that not all Ni^{2+} oxide species were reduced under these reduction conditions. This can be attributed to a strong MSI between Ni oxide and the respective TiO_2- and Nb_2O_5-containing SBA-15 supports, which was evidenced by the TPR characterization of the calcined catalysts (Figure 4). Resuming results from the XRD characterization, it can be noted that the dispersion of the reduced metallic Ni active phase improves with the addition of zirconia and alumina to the SBA-15 surface, while too strong metal-support interaction with titania- and niobia-containing SBA-15 supports allows us to obtain well-dispersed Ni particles but hinders the complete reduction of the NiO phase upon the reduction conditions used in the present work.

TEM images of the reduced Ni catalysts and the corresponding particle size distributions are shown in Figure 8. The average Ni particle sizes shown in this figure indicate that the Ni/SBA-15 catalyst presented the largest average particle size of Ni nanoparticles (11.6 nm), while the Ni catalysts supported on the M-SBA-15 (M = Ti, Zr, Al, and Nb) showed a smaller average size of the Ni active phase (between 6.4 and 9.4 nm). According to an increase in the Ni particles'

average size, the catalysts can be ordered as Ni/Ti-SBA-15 < Ni/Al-SBA-15 < Ni/Zr-SBA-15 < Ni/Nb-SBA-15 < Ni/SBA-15. An increase in the dispersion of metallic Ni in an order opposite to the above could be expected. In addition, the Ni/SBA-15 catalyst showed a wide particle size distribution (2 to 30 nm) with the presence of Ni particles larger in size than 25−30 nm on the external surface of the SBA-15 support. In comparison, the Ni catalysts supported on M-SBA-15 showed narrower particle size distributions (generally, 2−17 nm), with particles larger than 15 nm almost absent. This result once again confirmed an increase in the dispersion of the Ni active phase in the Ni/M-SBA-15 catalysts compared to the Ni/SBA-15 catalyst.

Additionally, a more detailed observation of the images shown in Figure 8 allows us to note in the image of the Ni/SBA-15 catalyst, Figure 8a, a very heterogeneous particle size distribution with the presence of large Ni particles outside the support's mesopores and some smaller particles that could be located inside of them. In the Ni/Ti-SBA-15 image, Figure 8b, small round-shaped Ni particles are seen, and it seems that the majority of them are on the external surface of the Ti-SBA-15 support (no particles inside the mesopores can be observed). On the contrary, for the reduced Ni/Zr-SBA-15 and Ni/Al-SBA-15 samples, Figure 8c,d, in addition to the Ni particles located on the external surface of the supports, Ni nanoparticles confined inside the Al- or Zr-SBA-15 mesopore channels can be observed (see particles inside the white circles in the images). The average size of the Ni nanoparticles in these two catalysts (7.1−8.7 nm) is close to the mesopore diameter of these catalysts, determined from N_2 adsorption isotherms (8.0−8.7 nm, Table 2). For the Ni/Nb-SBA-15 catalyst, the presence of Ni nanoparticles confined in the mesopores of the support was less notorious, Figure 8e,

although some of them could still be observed. There are some differences between the average particle sizes determined for the reduced catalysts from the TEM images (Figure 8) and the crystallite size of metallic Ni calculated based on the XRD data (Figure 7). However, both characterization techniques point out the same trend in an increase in the Ni particle size in the following order: Ni/Ti-SBA-15 < Ni/Al-SBA-15 < Ni/Zr-SBA-15 < Ni/Nb-SBA-15 < Ni/SBA-15.

Oxygen chemisorption was employed to determine the dispersion of the metallic Ni nanoparticles in the reduced catalysts and to estimate the amount of surface Ni atoms available for interaction with reactant molecules in HDO of anisole. The results from O_2 chemisorption are shown in Table 6. The dispersion of the Ni particles (D_{Ni}) was calculated

Table 6. Characteristics of Metallic Ni in Reduced Catalysts Determined by O_2 Chemisorption

catalyst	$Ni_{(T)}$ $(mmol_{Ni}/g_{cat})^a$	D_{Ni} $(\%)^b$	$Ni_{(S)}$ $(mmol_{Ni}/g_{cat})^c$
Ni/SBA-15	0.681	11.8	0.080
Ni/Ti-SBA-15	0.613	16.6	0.102
Ni/Zr-SBA-15	0.664	14.4	0.096
Ni/Al-SBA-15	0.647	16.4	0.106
Ni/Nb-SBA-15	0.681	14.4	0.098

$^a Ni_{(T)}$, total amount of nickel in the catalyst calculated based on real Ni loading (SEM−EDX). $^b D_{Ni}$, nickel dispersion calculated based on O_2 chemisorption results. $^c Ni_{(S)}$, nickel atoms located on the surface of Ni particles calculated based on the nickel dispersion determined by O_2 chemisorption.

based on the amount of chemisorbed O_2, and the experimental Ni loading in the catalysts was determined by SEM−EDX analysis (Table 1). The reduced catalysts showed similar dispersion values, between 11.8 and 16.6%, with the dispersion of Ni being slightly better on the M-SBA-15 supports compared to the SBA-15 one. The Ni/Ti-SBA-15 and Ni/Al-SBA-15 catalysts showed higher dispersion of Ni than other catalysts, which is in line with the smaller average particle sizes obtained for these catalysts by TEM measurements (Figure 8). The amount of Ni atoms located on the surface of Ni nanoparticles, $Ni_{(S)}$, was estimated based on the Ni dispersion values, D_{Ni}, and the total amount of Ni in each catalyst, $Ni_{(T)}$, also shown in Table 6. The amount of the surface Ni atoms calculated for the Ni/SBA-15 catalyst was 0.080 $mmol_{Ni}/g_{cat}$, while for the Ni/M-SBA-15 samples it varied between 0.096 $mmol_{Ni}/g_{cat}$ and 0.106 $mmol_{Ni}/g_{cat}$. The amount of $Ni_{(S)}$

surface species in the reduced catalysts increases as follows: Ni/SBA-15 < Ni/Zr-SBA-15 ≈ Ni/Nb-SBA-15 < Ni/Ti-SBA-15 ≈ Ni/Al-SBA-15. This result indicates that the addition of the selected metal oxides on the surface of the SBA-15 silica support produces a 20−30% increase in the amount of surface Ni.

3.3. Catalytic Activity in the HDO of Anisole. The catalytic performance of the reduced Ni catalysts was evaluated in HDO of anisole in a batch reactor at 280 °C and 4.8 MPa total pressure for 6 h. All Ni catalysts showed similar conversions of anisole, with only a ±5−8% difference along the catalytic activity tests, reaching the final conversions of anisole between 92 and 98%, Figure 9a. The highest conversion (98%) was obtained with the Ni/Zr-SBA-15 catalyst, followed by the Ni catalysts supported on Al-SBA-15, SBA-15, and Nb-SBA-15 (~95%), and finally, the Ni/Ti-SBA-15 catalyst, which exhibited the lowest anisole conversion (92%).

In spite of the similar catalytic activity of the synthesized catalysts in the consumption of anisole, their performance was notoriously different regarding the obtained reaction products (Figure 10). The main identified reaction products were cyclohexyl methyl ether (CME), cyclohexanol (CHL), and cyclohexane (CHA). Other reaction products such as methanol (MET), methyl cyclopentane (MCP), benzene (BEN), cyclohexene (CHE), methyl cyclohexane (MCH), and bicyclohexyl (BCH), were detected in small concentrations (<3%).

It is known that the reaction mechanism of anisole consists of different parallel/consecutive transformations that depend on the nature of the employed catalyst.[6,17,22,24,47−53] Thus, according to the distributions of products observed in the HDO of anisole in the present work (Figure 10) and taking into account that phenol (PHE) was not detected in the products, the formation of CHA could be achieved by the three parallel reaction pathways shown in the proposed mechanism (Scheme 1). In the first route, a cleavage of the $C_{aromatic}$−OCH$_3$ bond leads to the formation of BEN and MET. Subsequent hydrogenation of the obtained BEN gives CHA. In the second reaction route (2), first the aromatic ring of anisole is hydrogenated, producing CME, which consequently suffers demethoxylation (DMO), giving CHA. In the third reaction route (3), CHL is formed by a very quick hydrogenation of PHE, and its subsequent dehydroxylation (DHO) leads to CHA.
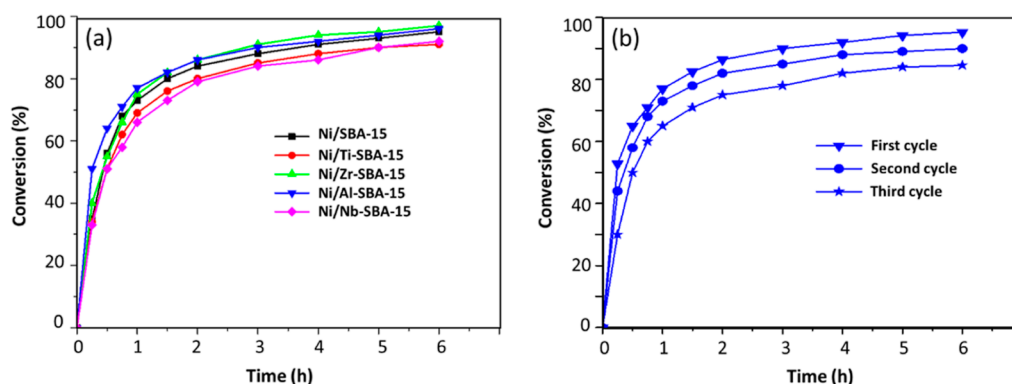

Figure 9. (a) Conversion of anisole over reduced Ni catalysts. (b) Conversions of anisole obtained with the Ni/Al-SBA-15 catalyst used in three reaction cycles. Reaction conditions: batch reactor, 280 °C temperature, 4.8 MPa total pressure, and 6 h reaction time.
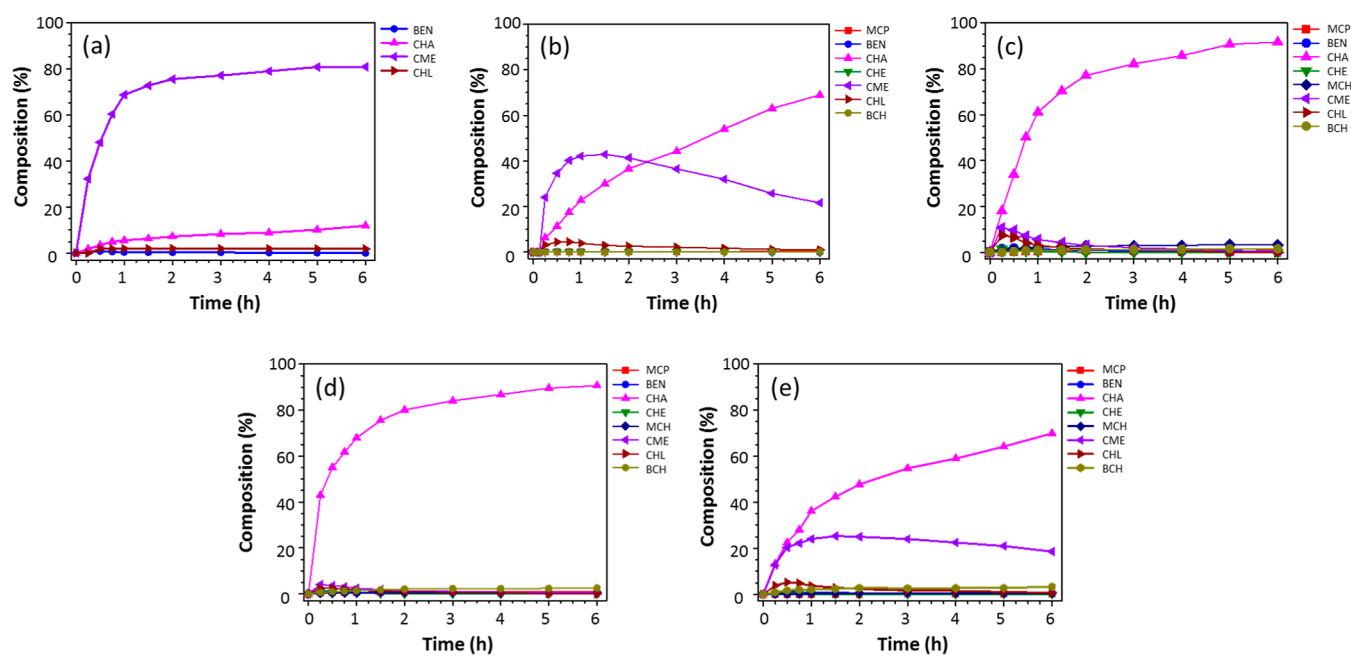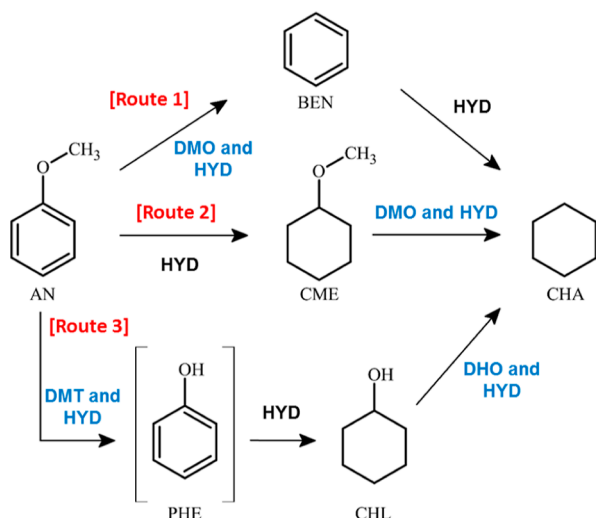
Figure 10. Reaction product compositions obtained with reduced catalysts: (a) Ni/SBA-15, (b) Ni/Ti-SBA-15, (c) Ni/Zr-SBA-15, (d) Ni/Al-SBA-15, and (e) Ni/Nb-SBA-15. Reaction conditions: batch reactor, 280 °C temperature, 4.8 MPa total pressure, 6 h reaction time.

Scheme 1. Reaction Mechanism Proposed for HDO of Anisole[a]

[a]DMO, demethoxylation; DMT, demethylation; DHO, dehydroxylation; HYD, hydrogenation; BEN, benzene; CME, cyclohexyl methyl ether; PHE, phenol; CHL, cyclohexanol; and CHA, cyclohexane. PHE was not detected in the products.

Among the three possible reaction pathways, the second and third routes seem to be more important than the first one. Thus, CME was detected as an intermediate product formed in a major amount with all the catalysts tested in the present work (Figure 10). CHL, an intermediate product of the third route, was also found in the reaction mixtures obtained with the catalysts supported on SBA-15 materials modified with different metal oxides (TiO$_2$, ZrO$_2$, Al$_2$O$_3$, and Nb$_2$O$_5$), Figure 10. However, it was formed only in a small amount (<2%) with the low acidity Ni/SBA-15 catalyst. These results point out to the fact that the ratio of the plausible reaction routes 2 and 3 depends on the acid characteristics of the

catalyst used. With the nonacidic catalysts, only the second route is favored, while the third route requires the presence of acid sites to facilitate the demethylation of anisole to PHE. On the other side, only small amounts of BEN (<1–2%) were detected in the products, making the first reaction route possible but not the principal one. This is in line with the C–O bond dissociation energy, which is ~100 kJ/mol higher for the aromatic alcohols (C$_{aromatic}$–O bonds) than for the non-aromatic secondary alcohols (C$_{aliphatic}$–O bonds).[6,53] In addition, the formation of small amounts of MCP (<1%), MCH (<3%), and BCH (<3%) was observed in the catalytic activity tests performed with the Ni/M-SBA-15 catalysts modified with different metal oxides (TiO$_2$, ZrO$_2$, Al$_2$O$_3$, and Nb$_2$O$_5$). These products were not obtained with the low-acidity Ni/SBA-15 catalyst, and they could be formed through different acid-catalyzed transformations. Thus, the MCP product could possibly be formed by the isomerization of the CHA ring during the decomposition of CHL or CME over B acid sites. On the other side, BCH could be obtained as a result of Friedel–Crafts alkylation of anisole with CHL and subsequent HDO.[54,55] MCH, in turn, could be originated from the disproportionation of anisole on acid sites with the formation of PHE and ortho- and para-methyl-anisole and HDO of the latter[56] or through the isomerization of anisole to cresol and further hydrogenation and deoxygenation. In addition, traces of CHE (<1%) were also detected. This reaction product could be formed by the dehydration of CHL on B acid sites.[49]

In addition to the different product distributions obtained with the tested Ni/(M)-SBA-15 catalysts, their selectivity to the final CHA product was also significantly different (Figure 11). Thus, the Ni/SBA-15 catalyst showed the lowest selectivity to CHA (~12% at 6 h reaction time) in comparison with the Ni/M-SBA-15 catalysts (70–90% at 6 h). These differences could be related to the acidity of the catalysts, namely, to the amount of medium and strong acid sites (Tables 4 and 5). Thus, the Ni/SBA-15 catalyst with the
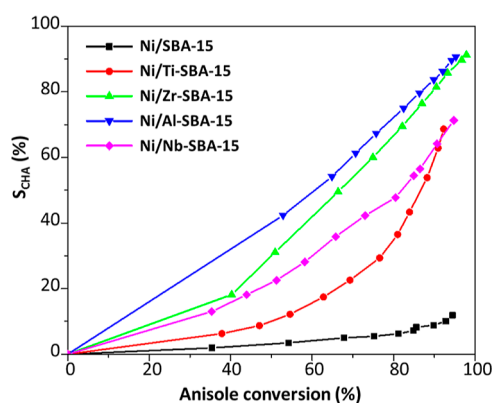
Figure 11. Selectivity to CHA (S_{CHA}) obtained with different catalysts as a function of anisole conversion. Reaction conditions: batch reactor, 280 °C temperature, 4.8 MPa total pressure, 6 h reaction time.

lowest amount of such acid sites showed the lowest CHA selectivity, while the Ni/Al-SBA-15 showed the highest CHA selectivity, followed by the Ni/Zr-SBA-15 one. At 6 h reaction time, both Ni/Al-SBA-15 and Ni/Zr-SBA-15 catalysts show similar S_{CHA} (~91%).

A mass balance approximation for the reactants and products present in the liquid phase was made by gas chromatography-liquid phase analysis (GCLPA, Table 7). Gaseous and heavy products (oligomerization products and carbonaceous solid precursors of coke deposits on the prepared catalysts) have not been quantified. As shown in Table 7, GCLPA values varied between 57.0 and 69.6% without a clear trend related to the acidity of the catalysts.

Table 7. Catalytic Activity of Reduced Ni/(M)-SBA-15 Catalysts in the HDO of Anisole

| catalyst	kinetic constants (h⁻¹)			estimated TOF values (h⁻¹)		GCLPA (%)[e]
	k_1[a]	k_2[b]	k_2/k_1	TOF_{AN}[c]	TOF_{C-O}[d]	
Ni/SBA-15	1.5	0.2	0.1	3150	170	68.9
Ni/Ti-SBA-15	1.3	0.8	0.6	2400	610	62.8
Ni/Zr-SBA-15	1.5	4.7	3.1	3000	1410	69.6
Ni/Al-SBA-15	1.7	22.2	13.1	3600	2880	57.0
Ni/Nb-SBA-15	1.4	2.2	1.6	2260	970	57.1
Mechanical Mixture						
Ni/SBA-15 + Al-SBA-15	1.1	4.3	3.9			

[a]k_1, pseudo-first order rate constant for hydrogenation of anisole (Scheme 2), calculated according to eq 4 using a curve-fitting method and anisole concentrations during the first hour of reaction time. [b]k_2, pseudo-first order rate constants for HDO of CME and CHL, calculated according to eqs 4−6 using a curve-fitting method and CME + CHL and CHA concentrations during the first hour of reaction time. [c]TOF_{AN}, turnover frequency for the hydrogenation of anisole (first step, Scheme 2), calculated on the basis of the initial rate of AN consumption (mmol/h) per mmol of $Ni_{(S)}$, sites determined by O_2 chemisorption (Table 6). [d]TOF_{C-O}, turnover frequency for the C−O hydrogenolysis of CME and CHL (second step, Scheme 2), calculated on the basis of the initial rate of CHA formation (mmol/h) per mmol of $Ni_{(S)}$, sites determined O_2 chemisorption (Table 6). [e]GCLPA is a mass balance approximation for the liquid phase. Theoretical GCLPA considering the complete transformation of anisole to CHA is 77.8%.

According to the obtained GCLPA results, the formation of some coke (ca. 10−20 wt %) can be expected in all the catalysts tested in the present work.

The most active catalyst (Ni/Al-SBA-15) was tested in three catalytic cycles for the HDO of anisole. After each reaction, the catalyst was separated by centrifugation and used again without any additional regeneration treatment. Obtained anisole conversions are shown in Figure 9b. It can be observed that final anisole conversions decreased from 95.3 to 90.0 and 84.6% in the second and third catalytic cycles, respectively. The above decrease in the catalytic activity of the used Ni/Al-SBA-15 catalyst could be ascribed to some mass loss of the catalyst upon separation after each reaction cycle and to deactivation due to coke formation, as shown by the obtained GCLPA results (Table 7). Therefore, the recycling of the catalysts such as those used in the present study would require some additional regeneration treatment for coke removal. On the other side, no leaching of the active Ni phase into the reaction mixture was detected.

For a more detailed kinetic analysis of the different reaction steps involved in the HDO of anisole (Scheme 1), we propose a simplified reaction mechanism based on the reaction routes 2 and 3 (Scheme 2). This mechanism consists of just two

Scheme 2. Simplified Lumped Reaction Mechanism Proposed for HDO of Anisole
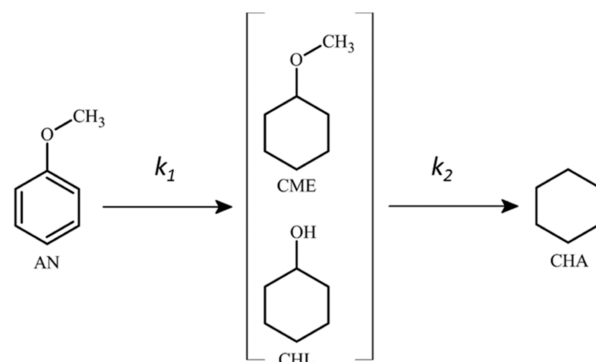
reaction steps: hydrogenation of anisole with the formation of oxygenated intermediates: CME and CHL, and their subsequent HDO to CHA. A similar reaction mechanism was proposed previously for anisole HDO over Ni-USY catalysts.[49] Proposing this mechanism, we assume that (i) there is no direct deoxygenation of anisole to CHA through BEN formation (route 1, Scheme 1, is insignificant); (ii) the proportion of CME and CHL changes depending on the catalyst, with CME being the main oxygenated intermediate for the low-acidity Ni/SBA-15 catalyst and CHL observed over Ni/M-SBA-15 samples (M = Ti, Zr, Al, and Nb); and (iii) DMO and DHO reactions both represent hydrogenolysis of $C_{aliphatic}$−O bond (HDO).

Following this simplified reaction scheme, the rate constants, k_1 and k_2, were calculated for the hydrogenation and HDO steps, respectively. Table 7 shows the obtained values of the reaction rate constants.

The rate constant k_1 showed values between 1.3 and 1.7 h⁻¹, being the lowest value for the Ni/Ti-SBA-15 catalyst and the highest value for the Ni/Al-SBA-15 catalyst. In general, the k_1 values increase as Ni/Ti-SBA-15 < Ni/Nb-SBA-15 < Ni/Zr-SBA-15 < Ni/SBA-15 < Ni/Al-SBA-15. A similar slight increase in the hydrogenation ability of Ni catalysts was

observed previously in the hydrogenation of naphthalene when SBA-15 support was modified by Al incorporation.[17] The variation in the k_1 values between the tested catalysts was about 1.3-fold indicating that the hydrogenation ability of the catalysts was only slightly influenced by the chemical composition of the (M)-SBA-15 support. Thus, the Ni/SBA-15 catalyst with the largest size of the metallic Ni nanoparticles (Figures 7 and 8 and Table 6) and a very low amount of acid sites (Tables 4 and 5) showed a good ability for the hydrogenation of the aromatic ring of anisole, almost similar to that of the Ni/Al-SBA-15 catalyst with the highest amount of medium and strong B and L acid sites (Table 5). In order to normalize the catalytic activity per number of surface Ni atoms (Ni sites available for the reaction) in different catalysts, the turnover frequency values were calculated for anisole hydrogenation (TOF_{AN}). For these calculations, results on Ni dispersion determined by the O_2 chemisorption were used ($Ni_{(S)}$, Table 6). All the tested catalysts showed TOF_{AN} values of the same order, between 2260 and 3600 h^{-1}, with the highest value for the Ni/Al-SBA-15 catalyst and the lowest for the Ni/Nb-SBA-15. No clear relationship was observed between the k_1 and TOF_{AN} values of different catalysts and their acid characteristics (Tables 4 and 5). Therefore, the variation of k_1 and TOF_{AN} values could be related mainly to the characteristics of the metallic Ni nanoparticles in the catalysts, such as, (i) different dispersion and average size of Ni nanoparticles (Table 6), (ii) some differences in their location inside or outside mesopore channels of the supports affecting an access to the Ni surface (TPR results, Figure 4), and (iii) the completeness of Ni reduction (XRD of reduced catalysts, Figure 7). Comparing results from Tables 6 and 7, it can be concluded that there is no clear relationship between the catalytic activity in hydrogenation (k_1 and TOF_{AN}) and the degree of dispersion of the metallic active phase in the catalysts (D_{Ni}). It seems that relatively large metal nanoparticles, such as in the reduced Ni/SBA-15 catalyst, have high hydrogenation ability. Regarding the last point, the low activity of the Ni/Ti-SBA-15 and Ni/Nb-SBA-15 catalysts in the hydrogenation of anisole could be attributed to the negative effect of the incomplete reduction of Ni oxide species in the activated catalysts (Figure 7). The above observations are in line with the previous report.[24]

On the other side, the k_2 rate constants corresponding to the HDO of CME and CHL to CHA showed more important differences in their values (Table 7). Thus, the Ni/SBA-15 catalyst showed the lowest k_2 value (0.2 h^{-1}), in accordance with the low production of CHA. On the other hand, the Ni/Ti-SBA-15 and Ni/Nb-SBA-15 catalysts exhibited ~4–11 times higher k_2 values than the respective Ni/SBA-15 catalyst. The Ni/Zr-SBA-15 and Ni/Al-SBA-15 catalysts showed even higher k_2 rate constants, 4.7 h^{-1} and 22.2 h^{-1}, respectively, 24 and ~110 times higher than the Ni/SBA-15 catalyst, respectively. These results are in line with the observed production of CHA and changes in the concentrations of the CME and CHL intermediates (Figure 10). The TOF_{C-O} values, calculated based on the amount of surface Ni atoms in the catalysts, represent the activity of one $Ni_{(S)}$ atom for the hydrogenolysis of $C_{aliphatic}$–O bond in CME and CHL (Table 7). These values varied between 170 h^{-1} for the Ni/SBA-15 catalyst and 2880 h^{-1} for the best one (Ni/Al-SBA-15) indicating a much higher hydrogenolysis ability of the latter catalyst. In this case, the differences in the k_2 and TOF_{C-O} values cannot be ascribed only to the differences in the

characteristics of the metallic Ni nanoparticles in the catalysts. They should also be related to the acid characteristics of the catalysts and the proximity of the metal and acid sites in them. Thus, it can be observed in Table 7 that the k_2 and TOF_{C-O} values follow the same trend as the amount of strong acid sites determined by TPD-NH$_3$ (Table 4) and medium and strong B + L acid sites determined by IR-Py (Table 5). Both increase in the following order: Ni/SBA-15 < Ni/Ti-SBA-15 < Ni/Nb-SBA-15 < Ni/Zr-SBA-15 < Ni/Al-SBA-15. This means that the amount of acid sites mentioned above in the catalysts affects the ability of the surface Ni atoms for hydrogenolysis of $C_{aliphatic}$–O bonds. As it has been reported previously,[24,57–59] the presence of proximal acid sites increases the activities of catalysts for C–O cleavage by a synergistic action. In addition, it can be noted in Tables 5 and 7 that the Ni/Al-SBA-15 and the Ni/Zr-SBA-15 catalysts, which showed high activity for HDO, not only have larger amounts of medium and strong B + L acid sites than other catalysts but also larger amounts of medium and strong B acid sites. It seems that the presence of such B acid sites promotes the hydrogenolysis of the $C_{aliphatic}$–O bond in CME (demethoxylation, DMO) and DHO/dehydration of the CHL intermediate, leading to the formation of CHA. In both cases, $C_{aliphatic}$–O bond cleavage through DMO or DHO is accompanied by the hydrogenation of the broken bonds on metallic active sites, and therefore, proximal (tandem) metal-acid active sites should be effective for these chemical transformations. On the other side, dehydration of CHL could take place on B acid sites, giving CHE, which could be further hydrogenated on metal active sites. In this case, metal and acid sites can function separately without near proximity.

4. DISCUSSION

4.1. On the Beneficial Effect of Bifunctional Metal-Acid Character of the Ni/M-SBA-15 Catalysts on HDO. In the present work, Ni catalysts supported on SBA-15 silica and M-SBA-15 supports modified with TiO$_2$, ZrO$_2$, Al$_2$O$_3$, or Nb$_2$O$_5$ were synthesized, characterized, and tested in the HDO of anisole. The best activity and selectivity to CHA results were obtained with the Ni/Al-SBA-15 and Ni/Zr-SBA-15 catalysts. These catalysts showed the presence of completely reduced Ni nanoparticles with a relatively good dispersion (Table 6), in addition to the presence of larger amounts of medium and strong B and L acid sites compared to those in other tested catalysts (Table 5). The good performance of the above two catalysts could be ascribed to their bifunctional character. Thus, it is known that a good catalyst for HDO should have active sites for oxygen activation and hydrogen dissociation.[60,61] In different works, the HDO of phenolic compounds over supported Ni catalysts reveals a high selectivity to CHA as a result of the presence of acid sites. Thus, Ni catalysts supported on USY zeolites tested for HDO of anisole showed higher rates of dehydration per acid site as a result of the proximity between Ni sites and a high amount of acid sites, resulting in higher selectivity to CHA. In contrast, the catalyst with few acid sites resulted in high selectivity to intermediate oxygenates (CME).[49] In the HDO of eugenol, high selectivity to propyl CHA (the hydrodeoxygenated product) was observed with the Ni/Al-SBA-15 catalyst, which was attributed to its stronger L acid sites.[37] In the HDO of DBF, performed on Ni/SBA-15 modified with aluminum, it was observed that the lowest Si/Al ratio (50) provided the most efficient catalyst for the formation of bicylohexyl, which was attributed to the
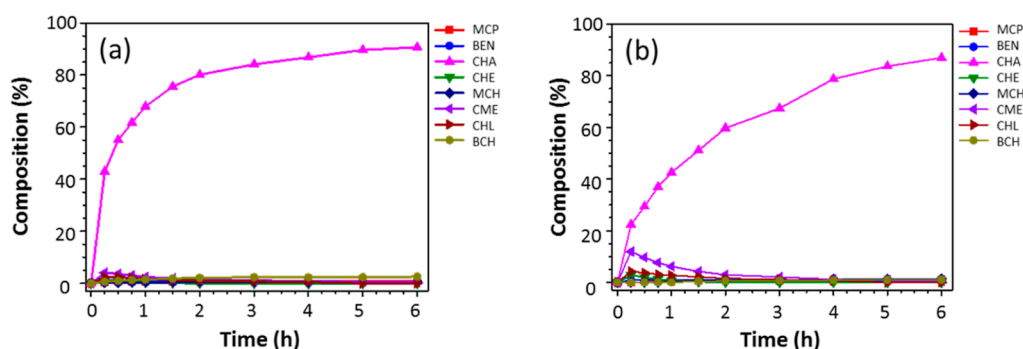
Figure 12. Reaction product compositions obtained with (a) Ni/Al-SBA-15 and (b) a mechanical mixture of Ni/SBA-15 + Al-SBA-15. Reaction conditions: batch reactor, 280 °C temperature, 4.8 MPa total pressure, 6 h reaction time.

more abundant acid sites.[25] For Ni catalysts supported on Al-SBA-15 and hierarchical ZSM-5 evaluated in HDO of anisole, a high conversion of anisole and selectivity to CHA (>90%) were observed as a result of the combination of Ni with acidic supports, while the Ni/SBA-15 catalyst showed selectivity to PHE (53%) and CHL (35%), caused by the nonacidic SBA-15 support.[24] According to the available literature information, amorphous mesoporous silicoaluminates or crystalline microporous zeolites were the most widely studied as supports for HDO catalysts compared to other mixed oxide materials with acid characteristics. The Ni/M-SBA-15 catalysts developed in the present work also showed a bifunctional metal-acid character, in which the metallic Ni sites are responsible for the hydrogenation of the aromatic ring (Scheme 1), while the acid sites play an important role in the $C_{aliphatic}$−O cleavage (deoxygenation step). The first hydrogenation step occurred quickly with all evaluated catalysts, while the second deoxygenation step was strongly related to their acid properties. Thus, deoxygenation was almost not observed with the Ni/SBA-15 catalyst due to the low acidity of this material. On the other side, the best CHA selectivity was obtained with the Ni/Al-SBA-15 catalysts (Figure 11) having the largest amount of medium and strong B and L acid sites, followed by the Ni/Zr-SBA-15 catalyst. A clear relationship can be observed between the (hydro)deoxygenation activity of the tested Ni/M-SBA-15 catalysts (k_2 and $TOF_{C−O}$ values) and the amount of medium and strong B + L acid sites (Tables 5 and 7). The Ni/Al-SBA-15 and Ni/Zr-SBA-15 showed higher $TOF_{C−O}$ values (2880 and 1410 h^{-1}, respectively) than other catalysts that could be correlated to the higher amounts of B + L acid sites in these catalysts (Table 5). In addition, the catalysts with a higher ability for $C_{aliphatic}$−O bond cleavage showed a larger amount of medium and strong B acid sites (Table 5), compared with other samples. This is in line with the previous observation that B acid sites are required for dehydration. Zhu et al.[59] found that B acid sites located near the Pt particles in Pt/H-Beta catalysts have shown synergistic effect on enhancing the HDO of anisole. In the HDO of PHE with Ni-HZSM-5 zeolite, the hydrogenation of the aromatic ring was executed by the Ni particles, followed by the dehydration that occurred on B acid sites.[62] Hewer et al.[47] observed in the HDO of anisole that HDO and hydro-dearomatization reactions with NiMo catalysts supported on SBA-15, SAPO-11, and γ-Al$_2$O$_3$, were strongly affected by the nature of the support, namely, by the relation of L and B acid sites present at the surface of these materials, modifying the products' distribution. 1-Methoxycyclohexane (═CME) and CHA were observed with SBA-15- and SAPO-11-supported

catalysts, while the NiMoAl sample exhibited mainly o-cresol and PHE products, suggesting that the hydrogenation of the aromatic ring is influenced by the acid sites of the supports.

4.2. Effect of the Proximity of Metal and Acid Sites on Their Behavior in HDO. Finally, in order to inquire into the effect of the proximity of the metallic Ni active sites and acid sites of the support on the activity and selectivity of the prepared bifunctional Ni/Al-SBA-15 catalyst, HDO of anisole was performed with a mechanical mixture of the Ni/SBA-15 catalyst and the Al-SBA-15 support. The Ni/Al-SBA-15 catalyst was selected because of its better activity and selectivity to CHA. For this purpose, the reduced Ni/SBA-15 catalyst (0.1 g) and the respective support (0.1 g) were put in the same reactor, and the reaction was performed under the same conditions as other HDO tests over Ni/M-SBA-15 catalysts.

Figure 12 shows a comparison of the reaction products obtained with the Ni/Al-SBA-15 catalyst and the corresponding mechanical mixture. It can be observed that in both cases, the same reaction products were obtained, although their yields were different. Higher amounts of reaction intermediates, CME and CHL, were observed over the mechanical mixture of the Ni/SBA-15 + Al-SBA-15 support in comparison with the Ni/Al-SBA-15 catalyst. This indicates that the transformation of the oxygenated intermediates to CHA becomes slower when metal and acid sites are separated, as in the mechanical mixture of the Ni/SBA-15 and Al-SBA-15 support.

Regarding the effect of the separation of metallic and acid sites on the catalytic activity at different steps of anisole HDO, the k_1 value of the mechanical mixture of the Ni/SBA-15 catalyst and Al-SBA-15 support was only 35% smaller than that of the corresponding Ni/Al-SBA-15 catalyst (1.1 vs 1.7 h^{-1}, Table 7). This can be ascribed to the adsorption of some anisole molecules (30−40% of the initial anisole concentration) on the acid sites of the Al-SBA-15 support as confirmed by an additional experiment in which the anisole solution was contacted with the Al-containing SBA-15 material upon the same reaction conditions. On the other hand, the k_2 value corresponding to the deoxygenation of CME and CHL intermediates decreased five times when Ni was deposited on the SBA-15, separately from the acid sites of the Al-SBA-15 material (4.3 vs 22.2 h^{-1}, respectively, Table 7). The above results clearly show that HDO of CME and CHL intermediates is favored on the catalysts, where metal and acid sites are located in close proximity, as in the Ni/Al-SBA-15 catalyst. This can be due to the fact that the steps of the reaction mechanism (Scheme 1), which involve the cleavage of

C−O bonds (DMO, DMT, and DHO) with the participation of acid sites, also comprise hydrogenation of the broken linkages on metallic active sites. Therefore, in line with previous reports,[49,58,59] the proximity of metal and acid sites in bifunctional catalysts gives rise to a synergy between them, making easier the cleavage of C−O bonds.

5. CONCLUSIONS

In the present work, SBA-15 materials modified with different metal oxides (TiO_2, ZrO_2, Al_2O_3, and Nb_2O_5) were employed as supports for the preparation of Ni catalysts, which were characterized and evaluated in the HDO of anisole. The characterization results showed that after the incorporation of the metal oxide on the bare SBA-15, its characteristic mesoporous structure and hexagonal arrangement of pores were preserved, as well as in the corresponding Ni catalysts. The chemical modification of the SBA-15 surface with Ti, Zr, Al, or Nb oxides increased acidity and metal-support interaction in the calcined catalysts, affecting the reducibility of NiO species. As a result, NiO was not completely reduced in the Ni/Ti-SBA-15 and Ni/Nb-SBA-15 catalysts upon activation at 400 °C for 4 h, explaining the lower activity of these two catalysts in the hydrogenation of the aromatic ring of anisole compared to other samples. On the other hand, the chemical composition and acidity of the M-SBA-15 support had a strong effect on the reaction product compositions obtained from the HDO of anisole. All the synthesized Ni/M-SBA-15 catalysts showed much higher selectivity to CHA compared to the Ni/SBA-15 catalyst that produced CME as the main product. The reaction rate constants (k_2) corresponding to HDO of CME and CHL intermediates increased in the following order: Ni/SBA-15 < Ni/Ti-SBA-15 < Ni/Nb-SBA-15 < Ni/Zr-SBA-15 < Ni/Al-SBA-15, which is in line with an increase in the amount of medium and strong acid sites. Among all the catalysts, the Ni/Al-SBA-15 and Ni/Zr-SBA-15 exhibited the best activity for HDO (k_2 and TOF_{C-O} values), as well as the highest selectivity to CHA (S_{CHA}). This can be attributed to a complete reduction of Ni oxide species in them and to the presence of medium-strong B acid sites that promote the formation of deoxygenated products via $C_{aliphatic}$−O bond scission. Finally, the importance of the proximity of the metal and acid sites was illustrated by a comparison of the catalytic behavior of the Ni/Al-SBA-15 catalyst and the mechanical mixture of the Ni/SBA-15 catalyst and the Al-SBA-15 support. The proximal metal-acid sites working in tandem improve the efficiency of the bifunctional catalysts for HDO and produce a synergistic effect.

ASSOCIATED CONTENT

Ⓢ Supporting Information

The Supporting Information is available free of charge at https://pubs.acs.org/doi/10.1021/acsomega.3c05865.

> SEM−EDX images of calcined NiO/(M)-SBA-15 catalysts, nitrogen adsorption−desorption isotherms and pore size distributions of calcined NiO/(M)-SBA-15 catalysts, SA-XRD patterns of supports and catalysts, TPD-NH$_3$ profiles of supports and catalysts, FT-IR spectra of pyridine adsorbed on the calcined NiO/(M)-SBA-15 catalysts (PDF)

AUTHOR INFORMATION

Corresponding Author

Tatiana E. Klimova − *Laboratorio de Nanocatálisis, Departamento de Ingeniería Química, Facultad de Química, Universidad Nacional Autónoma de México (UNAM), Cd. Universitaria, Ciudad de México CP 04510, Mexico;* ⓘ orcid.org/0000-0002-6623-6775; Phone: +52 55 56225371; Email: klimova@unam.mx

Authors

Lina A. Calzada − *Laboratorio de Nanocatálisis, Departamento de Ingeniería Química, Facultad de Química, Universidad Nacional Autónoma de México (UNAM), Cd. Universitaria, Ciudad de México CP 04510, Mexico*

Daniel Pérez-Estrada − *Laboratorio de Nanocatálisis, Departamento de Ingeniería Química, Facultad de Química, Universidad Nacional Autónoma de México (UNAM), Cd. Universitaria, Ciudad de México CP 04510, Mexico*

Miriam Sánchez-Ramírez − *Laboratorio de Nanocatálisis, Departamento de Ingeniería Química, Facultad de Química, Universidad Nacional Autónoma de México (UNAM), Cd. Universitaria, Ciudad de México CP 04510, Mexico*

Diana Gómora-Herrera − *Instituto Mexicano del Petróleo (IMP), Ciudad de México CP 07730, Mexico*

Antonio Gómez-Cortés − *Instituto de Física, Departamento de Física Química, Universidad Nacional Autónoma de México (UNAM), Ciudad de México CP 04510, Mexico*

Gabriela Díaz − *Instituto de Física, Departamento de Física Química, Universidad Nacional Autónoma de México (UNAM), Ciudad de México CP 04510, Mexico*

Complete contact information is available at:
https://pubs.acs.org/10.1021/acsomega.3c05865

Notes

The authors declare no competing financial interest.

REFERENCES

(1) Huber, G. W.; Iborra, S.; Corma, A. Synthesis of Transportation Fuels from Biomass: Chemistry, Catalysts, and Engineering. *Chem. Rev.* **2006**, *106*, 4044−4098.

(2) Robinson, A. M.; Hensley, J. E.; Medlin, J. W. Bifunctional Catalysts for Upgrading of Biomass-Derived Oxygenates: A Review. *ACS Catal.* **2016**, *6*, 5026−5043.

(3) Mäki-Arvela, P.; Murzin, D. Hydrodeoxygenation of Lignin-Derived Phenols: From Fundamental Studies towards Industrial Applications. *Catalysts* **2017**, *7*, 265.

(4) Dabros, T. M. H.; Stummann, M. Z.; Høj, M.; Jensen, P. A.; Grunwaldt, J.-D.; Gabrielsen, J.; Mortensen, P. M.; Jensen, A. D. Transportation fuels from biomass fast pyrolysis, catalytic hydro-deoxygenation, and catalytic fast hydropyrolysis. *Prog. Energy Combust. Sci.* **2018**, *68*, 268−309.

(5) Chen, S.; Zhou, G.; Miao, C. Green and renewable bio-diesel produce from oil hydrodeoxygenation: Strategies for catalyst development and mechanism. *Renewable Sustainable Energy Rev.* **2019**, *101*, 568−589.

(6) Mortensen, P. M.; Grunwaldt, J.-D.; Jensen, P. A.; Jensen, A. D. Screening of Catalysts for Hydrodeoxygenation of Phenol as a Model Compound for Bio-oil. *ACS Catal.* **2013**, *3*, 1774−1785.

(7) González, C.; Marín, P.; Díez, F. V.; Ordóñez, S. Gas-phase hydrodeoxygenation of benzaldehyde, benzyl alcohol, phenyl acetate, and anisole over precious metal catalysts. *Ind. Eng. Chem. Res.* **2016**, *55*, 2319−2327.

(8) Gao, D.; Xiao, Y.; Varma, A. Guaiacol Hydrodeoxygenation over Platinum Catalyst: Reaction Pathways and Kinetics. *Ind. Eng. Chem. Res.* **2015**, *54*, 10638−10644.

(9) Ohta, H.; Yamamoto, K.; Hayashi, M.; Hamasaka, G.; Uozumi, Y.; Watanabe, Y. Low temperature hydrodeoxygenation of phenols under ambient hydrogen pressure to form cyclohexanes catalysed by Pt nanoparticles supported on H-ZSM-5. *Chem. Commun.* **2015**, *51*, 17000−17003.

(10) Teles, C. A.; Rabelo-Neto, R. C.; Jacobs, G.; Davis, B. H.; Resasco, D. E.; Noronha, F. B. Hydrodeoxygenation of Phenol over Zirconia-Supported Catalysts: The Effect of Metal Type on Reaction Mechanism and Catalyst Deactivation. *ChemCatChem* **2017**, *9*, 2850−2863.

(11) Szczyglewska, P.; Feliczak-Guzik, A.; Nowak, I. A support effect on the hydrodeoxygenation reaction of anisole by ruthenium catalysts. *Microporous Mesoporous Mater.* **2020**, *293*, 109771.

(12) Valdés-Martínez, O.; Suárez-Toriello, V.; Reyes, J. d. l.; Pawelec, B.; Fierro, J. L. G. Support effect and metals interactions for NiRu/Al$_2$O$_3$, TiO$_2$ and ZrO$_2$ catalysts in the hydrodeoxygenation of phenol. *Catal. Today* **2017**, *296*, 219−227.

(13) Lang, M.; Li, H. Heterogeneous metal-based catalysts for cyclohexane synthesis from hydrodeoxygenation of lignin-derived phenolics. *Fuel* **2023**, *344*, 128084.

(14) Feng, S.; Liu, X.; Su, Z.; Li, G.; Hu, C. Low temperature catalytic hydrodeoxygenation of lignin-derived phenols to cyclohexanols over the Ru/SBA-15 catalyst. *RSC Adv.* **2022**, *12*, 9352−9362.

(15) Teles, C. A.; Ciotonea, C.; Gomes, N.; Gonçalves, V. O.; Ungureanu, A.; Catrinescu, C.; Marinova, M.; Clacens, J.-M.; Royer, S.; Noronha, F. B.; Richard, F. Hydrodeoxygenation of m-cresol over Pd/Al-SBA-15 catalysts: Effect of Al content on the deoxygenation reaction pathways. *Appl. Catal., A* **2022**, *641*, 118686.

(16) Wang, X. Y.; Rinaldi, R. Exploiting H-transfer reactions with RANEY® Ni for upgrade of phenolic and aromatic biorefinery feeds under unusual, low-severity conditions. *Energy Environ. Sci.* **2012**, *5*, 8244−8260.

(17) Vargas-Villagrán, H.; Ramírez-Suárez, D.; Ramírez-Muñoz, G.; Calzada, L. A.; González-García, G.; Klimova, T. E. Tuning of activity and selectivity of Ni/(Al)SBA-15 catalysts in naphthalene hydrogenation. *Catal. Today* **2021**, *360*, 27−37.

(18) Yu, X.; Williams, C. T. Recent advances in the applications of mesoporous silica in heterogeneous catalysis. *Catal. Sci. Technol.* **2022**, *12*, 5765−5794.

(19) Singh, S.; Kumar, R.; Setiabudi, H. D.; Nanda, S.; Vo, D.-V. N. Advanced synthesis strategies of mesoporous SBA-15 supported catalysts for catalytic reforming applications: A state-of-the-art review. *Appl. Catal., A* **2018**, *559*, 57−74.

(20) Calles, J. A.; Carrero, A.; Vizcaíno, A. J.; García-Moreno, L.; Megía, P. J. Steam Reforming of Model Bio-Oil Aqueous Fraction Using Ni-(Cu, Co, Cr)/SBA-15 Catalysts. *Int. J. Mol. Sci.* **2019**, *20*, 512−533.

(21) Ochoa-Hernández, C.; Yang, Y.; Pizarro, P.; de la Peña O'Shea, V. A.; Coronado, J. M.; Serrano, D. P. Hydrocarbons production through hydrotreating of methyl esters over Ni and Co supported on SBA-15 and Al-SBA-15. *Catal. Today* **2013**, *210*, 81−88.

(22) Jin, S.; Xiao, Z.; Li, C.; Chen, X.; Wang, L.; Xing, J.; Li, W.; Liang, C. Catalytic hydrodeoxygenation of anisole as lignin model compound over supported nickel catalysts. *Catal. Today* **2014**, *234*, 125−132.

(23) Yang, Y.; Ochoa-Hernández, C.; de la Peña O'Shea, V. A.; Pizarro, P.; Coronado, J. M.; Serrano, D. P. Effect of metal-support interaction on the selective hydrodeoxygenation of anisole to aromatics over Ni-based catalysts. *Appl. Catal., B* **2014**, *145*, 91−100.

(24) Sankaranarayanan, T. M.; Berenguer, A.; Ochoa-Hernández, C.; Moreno, I.; Jana, P.; Coronado, J. M.; Serrano, D. P.; Pizarro, P. Hydrodeoxygenation of anisole as bio-oil model compound over supported Ni and Co catalysts: Effect of metal and support properties. *Catal. Today* **2015**, *243*, 163−172.

(25) Gbadamasi, S.; Ali, T. H.; Voon, L. H.; Atta, A. Y.; Sudarsanam, P.; Bhargava, S. K.; Abd Hamid, S. B. Promising Ni/Al-SBA-15 catalysts for hydrodeoxygenation of dibenzofuran into fuel grade hydrocarbons: synergetic effect of Ni and Al-SBA-15 support. *RSC Adv.* **2016**, *6*, 25992−26002.

(26) Li, X.; Liu, J.; Zhang, J.; Liu, B.; Ma, W.; Wang, C.; Chen, G. Effect of nickel loading approaches on the structure and hydrodeoxygenation performance of Ni/Al-SBA-15. *Cellulose* **2019**, *26*, 8301−8312.

(27) Li, X.; Chen, L.; Chen, G.; Zhang, J.; Liu, J. The relationship between acidity, dispersion of nickel, and performance of Ni/Al-SBA-15 catalyst on eugenol hydrodeoxygenation. *Renewable Energy* **2020**, *149*, 609−616.

(28) Ballesteros-Plata, D.; Barroso-Martín, I.; Medina Cervantes, J. A.; Maciel, C.; Huirache-Acuña, R.; Rodríguez-Castellón, E.; Infantes-Molina, A. Bimetallic Niobium-Based Catalysts Supported on SBA-15 for Hydrodeoxygenation of Anisole. *Ind. Eng. Chem. Res.* **2021**, *60*, 18831−18840.

(29) López, M.; Palacio, R.; Mamede, A.-S.; Fernández, J. J.; Royer, S. Hydrodeoxygenation of guaiacol into cyclohexane over mesoporous silica supported Ni-ZrO$_2$ catalyst. *Microporous Mesoporous Mater.* **2020**, *309*, 110452.

(30) Zhao, D.; Feng, J.; Huo, Q.; Melosh, N.; Fredrickson, G. H.; Chmelka, B. F.; Stucky, G. D. Triblock copolymer syntheses of mesoporous silica with periodic 50 to 300 angstrom pores. *Science* **1998**, *279*, 548−552.

(31) Hughes, T. R.; White, H. M. A Study of the Surface Structure of Decationized Y Zeolite by Quantitative Infrared Spectroscopy. *J. Phys. Chem.* **1967**, *71*, 2192−2201.

(32) Emeis, C. A. Determination of Integrated Molar Extinction Coefficients for Infrared Absorption Bands of Pyridine Adsorbed on Solid Acid Catalysts. *J. Catal.* **1993**, *141*, 347−354.

(33) Pardue, H. L. Kinetic Aspects of Analytical Chemistry. *Anal. Chim. Acta* **1989**, *216*, 69−107.

(34) Klimova, T.; Gutiérrez, O.; Lizama, L.; Amezcua, J. Advantages of ZrO$_2$-and TiO$_2$-SBA-15 mesostructured supports for hydrodesulfurization catalysts over pure TiO$_2$, ZrO$_2$ and SBA-15. *Microporous Mesoporous Mater.* **2010**, *133*, 91−99.

(35) Rodriguez-Gomez, A.; Caballero, A. Identification of Outer and Inner Nickel Particles in a Mesoporous Support: How the Channels Modify the Reducibility of Ni/SBA-15 Catalysts. *Chem. Nanomater.* **2017**, *3*, 94−97.

(36) Kong, X.; Zhu, Y.; Zheng, H.; Li, X.; Zhu, Y.; Li, Y.-W. Ni Nanoparticles Inlaid Nickel Phyllosilicate as a Metal-Acid Bifunctional Catalyst for Low-Temperature Hydrogenolysis Reactions. *ACS Catal.* **2015**, *5*, 5914−5920.

(37) Li, X.; Zhang, J.; Liu, B.; Liu, J.; Wang, C.; Chen, G. Hydrodeoxygenation of lignin-derived phenols to produce hydrocarbons over Ni/Al-SBA-15 prepared with different impregnants. *Fuel* **2019**, *243*, 314−321.

(38) Robertson, J. J. Band offsets of wide-band-gap oxides and implications for future electronic devices. *J. Vac. Sci. Technol., B: Microelectron. Nanometer Struct.–Process., Meas., Phenom.* **2000**, *18*, 1785−1791.

(39) French, R. H. Electronic Band Structure of Al$_2$O$_3$, with Comparison to Alon and AIN. *J. Am. Ceram. Soc.* **1990**, *73*, 477−489.

(40) Méndez, F. J.; Franco-López, O. E.; Bokhimi, X.; Solís-Casados, D. A.; Escobar-Alarcón, L.; Klimova, T. E. Dibenzothiophene

hydrodesulfurization with NiMo and CoMo catalysts supported on niobium-modified MCM-41. *Appl. Catal., B* **2017**, *219*, 479−491.

(41) Morey, M. S.; Stucky, G. D.; Schwarz, S.; Fröba, M. Isomorphic Substitution and Postsynthesis Incorporation of Zirconium into MCM-48 Mesoporous Silica. *J. Phys. Chem. B* **1999**, *103*, 2037−2041.

(42) Akhverdiev, R.; Abad-zade, K.; Krylov, O.; Rustamov, M. Investigation of the valence and coordination state of nickel ions in zeolite-containing catalysts by diffuse reflectance spectroscopy. *Kinet. Catal.* **1985**, *26*, 327−331.

(43) Chen, B.-H.; Chao, Z.-S.; He, H.; Huang, C.; Liu, Y.-J.; Yi, W.-J.; Wei, X.-L.; An, J.-F. Towards a full understanding of the nature of Ni(II) species and hydroxyl groups over highly siliceous HZSM-5 zeolite supported nickel catalysts prepared by a deposition-precipitation method. *Dalton Trans.* **2016**, *45*, 2720−2739.

(44) Ganiyu, S. A.; Alhooshani, K. Catalytic Performance of NiMoS Supported on (Zr)SBA-15 for Hydrodesulfurization of Diesel: Insight into a One-Step Calcination and Reduction Strategy during Sulfidation. *Energy Fuels* **2019**, *33*, 3047−3056.

(45) Zhang, D.; Duan, A.; Zhao, Z.; Wang, X.; Jiang, G.; Liu, J.; Wang, C.; Jin, M. Synthesis, characterization and catalytic perform-ance of meso-microporous material Beta-SBA-15-supported NiMo catalysts for hydrodesulfurization of dibenzothiophene. *Catal. Today* **2011**, *175*, 477−484.

(46) Penkova, A.; Bobadilla, L. F.; Romero-Sarria, F.; Centeno, M. A.; Odriozola, J. A. Pyridine adsorption on NiSn/MgO-Al$_2$O$_3$: An FTIR spectroscopic study of surface acidity. *Appl. Surf. Sci.* **2014**, *317*, 241−251.

(47) Hewer, T. L. R.; Souza, A. G. F.; Roseno, K. T. C.; Moreira, P. F.; Bonfim, R.; Alves, R. M. B.; Schmal, M. Influence of acid sites on the hydrodeoxygenation of anisole with metal supported on SBA-15 and SAPO-11. *Renewable Energy* **2018**, *119*, 615−624.

(48) Khromova, S. A.; Smirnov, A. A.; Bulavchenko, O. A.; Saraev, A. A.; Kaichev, V. V.; Reshetnikov, S. I.; Yakovlev, V. A. Anisole hydrodeoxygenation over Ni-Cu bimetallic catalysts: The effect of Ni/Cu ratio on selectivity. *Appl. Catal., A* **2014**, *470*, 261−270.

(49) Gamliel, D. P.; Baillie, B. P.; Augustine, E.; Hall, J.; Bollas, G. M.; Valla, J. A. Nickel impregnated mesoporous USY zeolites for hydrodeoxygenation of anisole. *Microporous Mesoporous Mater.* **2018**, *261*, 18−28.

(50) Lee, H.; Kim, H.; Yu, M. J.; Ko, C. H.; Jeon, J.-K.; Jae, J.; Park, S. H.; Jung, S.-C.; Park, Y.-K. Catalytic Hydrodeoxygenation of Bio-oil Model Compounds over Pt/HY Catalyst. *Sci. Rep.* **2016**, *6* (1), 28765.

(51) Sudhakar, P.; Pandurangan, A. Pt/Ni wet impregnated over Al incorporated mesoporous silicates: a highly efficient catalyst for anisole hydrodeoxygenation. *J. Porous Mater.* **2018**, *25*, 747−759.

(52) Li, F.-X.; Wang, X.-F.; Zheng, Y.; Chen, J.-X. Influence of metallic promoters on the performance of Ni/SiO$_2$ catalyst in the hydrodeoxygenation of anisole. *J. Fuel Chem. Technol.* **2018**, *46*, 75−83.

(53) Ghampson, I. T.; Canales, R.; Escalona, N. A study of the hydrodeoxygenation of anisole over Re-MoO$_x$/TiO$_2$ catalyst. *Appl. Catal., A* **2018**, *549*, 225−236.

(54) Ramanathan, A.; Zhu, H.; Maheswari, R.; Subramaniam, B. Novel zirconium containing cage type silicate (Zr-KIT-5): An efficient Friedel-Crafts alkylation catalyst. *Chem. Eng. J.* **2015**, *278*, 113−121.

(55) Li, S.; Zhou, H.; Jin, C.; Feng, N.; Liu, F.; Deng, F.; Wang, J.-Q.; Huang, W.; Xiao, L.; Fan, J. Formation of Subnanometer Zr-WOx Clusters within Mesoporous W-Zr Mixed Oxides as Strong Solid Acid Catalysts for Friedel-Crafts Alkylation. *J. Phys. Chem. C* **2014**, *118*, 6283−6290.

(56) Pichot, N.; Hounfodji, J. W.; Badawi, M.; Valtchev, V.; Mintova, S.; Gilson, J.-P.; Dufour, A.; Pinard, L. Products and coke shape-selectivity during anisole disproportionation over HZSM-5. *Appl. Catal., A* **2023**, *665*, 119352.

(57) Shivhare, A.; Hunns, J. A.; Durndell, L. J.; Parlett, C. M. A.; Isaacs, M. A.; Lee, A. F.; Wilson, K. Metal-Acid Synergy: Hydrodeoxygenation of Anisole over Pt/Al-SBA-15. *ChemSusChem* **2020**, *13*, 4945−4953.

(58) Song, W.; Liu, Y.; Baráth, E.; Zhao, C.; Lercher, J. A. Synergistic effects of Ni and acid sites for hydrogenation and C-O bond cleavage ofsubstituted phenols. *Green Chem.* **2015**, *17*, 1204−1218.

(59) Zhu, X.; Lobban, L. L.; Mallinson, R. G.; Resasco, D. E. Bifunctional transalkylation and hydrodeoxygenation of anisole over a Pt/HBeta catalyst. *J. Catal.* **2011**, *281*, 21−29.

(60) Mortensen, P. M.; Grunwaldt, J.-D.; Jensen, P. A.; Knudsen, K. G.; Jensen, A. D. A review of catalytic upgrading of bio-oil to engine fuels. *Appl. Catal., A* **2011**, *407*, 1−19.

(61) Ju, C.; Li, M.; Fang, Y.; Tan, T. Efficient hydro-deoxygenation of lignin derived phenolic compounds over bifunctional catalysts with optimized acid/metal interactions. *Green Chem.* **2018**, *20*, 4492−4499.

(62) Zhao, C.; Kasakov, S.; He, J.; Lercher, J. A. Comparison of kinetics, activity and stability of Ni/HZSM-5 and Ni/Al$_2$O$_3$-HZSM-5 for phenol hydrodeoxygenation. *J. Catal.* **2012**, *296*, 12−23.